Chapter 1
Introduction

When an optical field interacts with a structure of geometric features comparable (or smaller) to the optical wavelength, the near-field distribution of the light wave varies significantly at the sub wavelength scales. There are numerous opportunities for advanced functionalities with smaller device structures. Therefore recently sub optical wavelength (SOW) devices have attracted significantly research interest.

However the use of the classical diffraction theory, which simplifies the problem and allows for approximate solutions, is not appropriate for the design of SOW devices. The rapid variation of the light field in SOW devices makes the design and analysis of SOW devices difficult.

Global optimization is a task of finding a set of parameters to optimize an objective function (cost function). In this thesis, we explore the possibility and method to effectively combine global optimization algorithms with a device simulator for the design of sub-wavelength devices. We show in this study that the approach not only allows us to retrieve the optimal structure of a SOW device but also from the result to deduce the operation principle of the device.

In chapter 2 of this thesis, we introduce some useful global optimization algorithms, which are to be used for this study. We first evaluate these global

optimization procedures by using a multi-extrema function. The influences with different cost functions on searching speed and searching results of global optimizers are also presented in this chapter.

After introducing the global optimizers, in chapter 3 we apply the methodology for the designs and analyses of four SOW devices. There are three motivations to apply global optimizer for the design of SOW device: (1) to yield better device performance with less fabrication resource; (2) to verify the conjecture of the device operation principle; and (3) by examining the optimal result, we can construct a device model and retrieve some design rules. In each case presented in Chapter 3, we shall follow this strategy to fulfill our goal.

Beam propagation method (BPM), eigenmode expansion method, and finite-difference time-domain (FDTD) method are the three most useful solvers for the simulation of SOW device. FDTD is an ideal candidate for SOW device simulation. However, it takes too much time to complete one simulation. In the process of global optimization of device structure, we need to perform several thousand times of device simulation in order to discover the optimal structure. Therefore FDTD is suitable for global optimization only when highly sophisticated computing resource is available. Beam propagation method is also not an appropriate choice for the simulation of SOW devices in view of its assumption of slowly varying envelope. For this research we make our best judge by choosing the eigenmode expansion method as our device simulator.

In chapter 4, to explore the possible ways to probe the anisotropic response of optical field from sub optical wavelength structure we perform an experimental study

for the measurement of magneto-optical Kerr effect from nanostructured material. We can deduce information about the refractive index variation (or birefringence) of a sample from the polarization state of the reflected light. By combining with an appropriate optical microscopy, we believe this method can measure MOKES or form birefringence of SOW device. Kerr rotation of magneto-optical effect is very small (10^{-5}~10^{-4} radian for ferromagnetism material) and the measurement is fairly difficult and we report a successful approach to measure Kerr rotation from the magneto-optical Kerr effect of a film of Co^{2+}:doped ZnO quantum dots.

Chapter 2
Overview of Global Optimization Methodology

In this chapter, we shall review some optimization methods, which are useful for solving optimization problem of SOW device. In Section 2.1, we first categorize optimization method into two classes: local search and global search. We then in Section 2.2 discuss the searching capabilities and characteristics of some useful global optimization methods. We evaluate these methods in Section 2.3 based on their search characteristics with a multi-extrema function. These global optimization methods will be employed in Chapter 3 for the optimal designs of sub-wavelength optical devices.

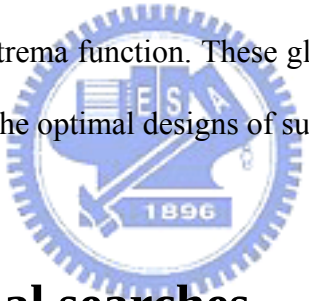

2.1 local and global searches

Local search method is usually implemented with the algorithm of generalized reduced gradient. This algorithm is simple and can easily approach a local extremum. For this reason, local search method is the ideal solver for a function with single extremum. Since local search method can yield precise solution of local extremum, it is usually implemented in the last searching phase of an optimization problem.

Methods of global search are not based on the assumption of single extremum; therefore they can be used to solve a variety of optimization problems with multiple extrema. Many algorithms have been developed for a successful global search. We can categorize the current global optimization techniques into the following methods:

- set (space) covering techniques;
- random search methods;
- methods based on multiple local searches (*i.e.*, multi-start);
- evolutionary and genetic algorithm;

Many physical systems generate their outputs continuously with inputs. The corresponding optimization problem is therefore called as continuous problem. Therefore in this chapter, we shall limit our discussion to the continuous problems.

2.2 Global search methods

In this section, we review the global optimization algorithms that are to be employed in chapter 3 for the optimal design of sub-wavelength optical devices.

We implement each global optimization method as a combination of different global search methods and a local search in the final searching phase. The global search methods used in this thesis are branch-and-bound global method (BB), global adaptive random search (GARS), and multi-start based global random search (MS).

2.2.1 Global adaptive random search (GARS)

Random search algorithm had already been broadly applied in many optimization problems. By using different sampling approach, random search can be implemented into different versions, which include pure direct random search, adaptive random search, and controlled random search.

The typical structure of random search method can be shown by the following search steps (a flow chart is drawn in Fig. 2.1 to facilitate the discussion):

Step 1. Choose a starting point x^0. Here subscript 0 indicates the number of iteration k=0.

Step 2. Generate one new trial point with $y^k = x^k + r^k$, where r^k denotes a random vector.

Step 3. Determine next generation point x^k (*i.e.* x^{k+1}) according to some appropriate rules such as

$$x^k = \begin{cases} y^k, \text{if } f(y^k) < f(x^k) \\ x^k, \text{ otherwise} \end{cases}, \tag{2-1}$$

where $f(x)$ is the function that we want to determine its extrema.

Step 4. Stop when the stopping criterion is satisfied. Otherwise: set $k = k + 1$, and go to Step 1 and repeat the procedures.

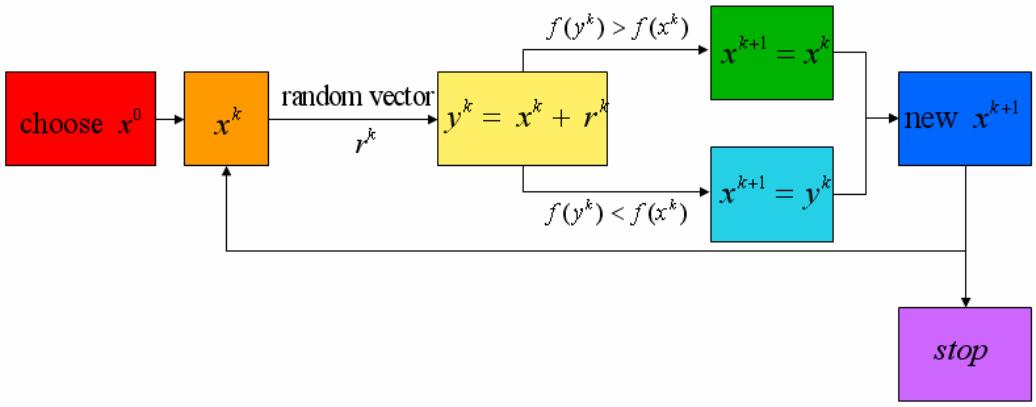

Fig 2.1: Flow chart of a typical random search method.

Step 3 is the most critical step to ensure that $f(x^k)$ becomes smaller with an increasing iteration number k. This also warrantees proper performance for different random search schemes. Different versions of random search methods differ in the choice of random vector r^k and the rule used in Step 3. For example, when the choice of random vector r^k depends on the set of $f(x^0)$, $f(x^1)$, $f(x^k)$, we call the resulting method adaptive random search (ARS).

A simple idea can be proposed for adaptive random search. At the beginning of optimization, the x^k may be far from the solution x^*. So we can choose r^k with a

large variance. This makes x^k distributed over a large domain. After several iterations, x^k is close to x^*. A smaller variance of r^k is preferred for more detailed search. In this method, adaptive random search (ARS) can adaptively reduce the searching region, and gradually focuses on the region where the global optimum point is located.

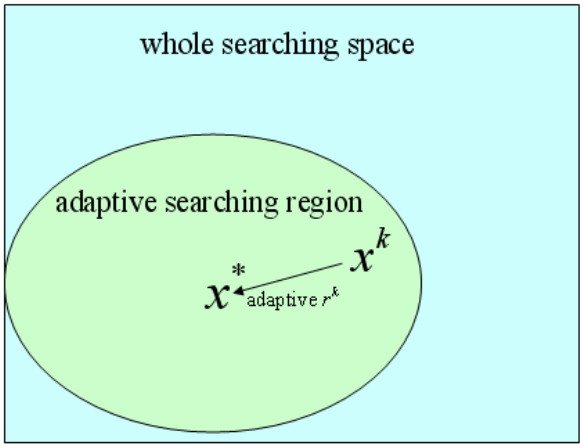

Fig. 2.2: By going through successive search steps, GARS decreases the distance between x^k and x^* as the iteration number increases and the searching region is accordingly reduced.

2.2.2 Multi-start global random search

The basic idea of the so-called multi-start methods is to apply local search procedure several times in order to discover several local minima. The solver then selects the best one among these extrema and considers it to be the global minimum.

Multi-start methods can be implemented by the following procedures:

Step1: From the searching space, arbitrarily select several points and compute their function values.

Step2: Select several "most promising points" from *step 1*, and start local search procedure in order to discover the point with the least value.

Step3: Determine whether to stop or to return to Step 1 based on whether the stopping

criterion is satisfied or not. If the criterion is satisfied, determine the global minimum.

Multi-start global random search algorithm can also be implemented with the adaptive random search to replace the Step-1 and Step-2. The framework of the adaptive random search and multi-start random search are very similar. However, multi-start global random search spends more effort on multi-searches. The flow chart of multi-start random search is shown in Fig. 2.3. Comparing with the adaptive random search presented in 2.2.3, we can rapidly reduce the searching region in global search phase and therefore greatly save the search time. Besides, comparing with strict search, it also prevents the global optimizer from sticking on some local extrema points.

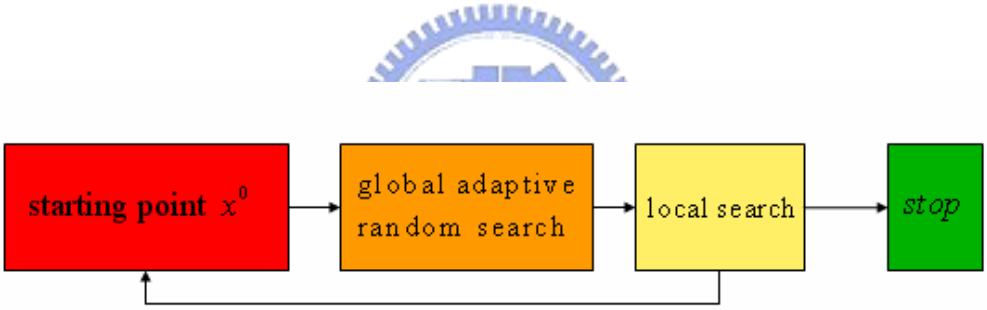

Fig. 2.3: Flow chart of multi-start based global random search.

2.2.3 Branch-and-bound search method (BB)

Branch-and-bound (BB) algorithm [1] has been widely used to solve various kinds of difficult optimization problems. This technique splits the feasible set into several subsets (*i.e.*, the branch). The bounds (lower and upper bound) of each subset are then estimated to determine next feasible regions. The procedures are repeated to achieve the final global extremum. The main idea of BB method can be implemented in the following:

- Start from a searching space and split the entire domain into a series of subsets.

- For each subset determine its lower (β) and upper(α) bounds, respectively.

- If $\beta = \alpha$, then stop.

According to the idea, the flow chart of a BB optimizer can be depicted in Fig. 2.4. Here the lower and upper bounds are the lower and upper limit of *f*(x) in a specific subset. If we know the lower and upper bounds, in principle we can estimate the minimum value of *f*(x). However, it is sometime problematic to find them.

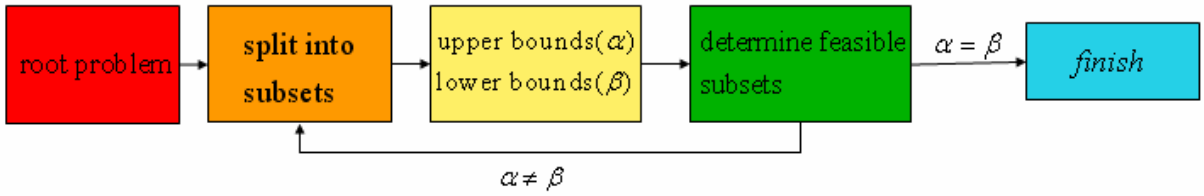

Fig 2.4: Flow chart of branch and bound search method.

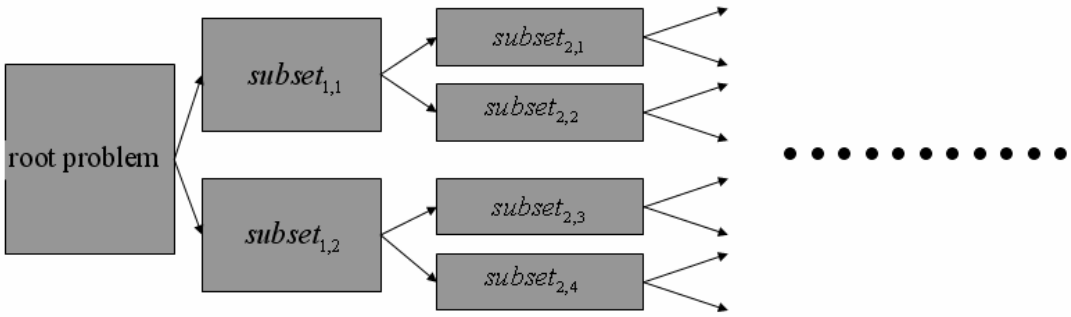

Fig 2.5: A feasible set is split into parts. By subsequently determining the next feasible subsets, we can reduce the searching region and finally approach to the globally optimal solution.

The proper method to obtain the lower and upper bounds usually depends on the optimization problem that are solving. When we deal with a continuous function, the upper bounds can be easily set to the minimum value of the function. We can also

determine the maximum 'slope' of *f*(x) (denoted as A) in the same way. Thus the lower bound $\beta = \max\{f(x) : x \text{ on the boundary of subset}\} - A\delta$, where δ denotes the diameter of the subset. By comparing the lower and upper bounds among the subsets, we can determine the feasible subsets. In this way, we can reduce our searching region, and gradually approach to the global minimum.

2.3 Test run with an analytical function

In order to analyze the searching characteristics and capabilities of global optimization methods, in this section we construct an appropriate function:

$$\begin{aligned} f(a,b) = {} & (1-0.3\cdot 10^{-3(|a-0.166|+|b-0.166|)})(1-0.34\cdot 10^{-6(|a-0.5|+|b-0.166|)})(1-0.38\cdot 10^{-9(|a-0.833|+|b-0.166|)}) \\ & \times(1-0.42\cdot 10^{-12(|a-0.166|+|b-0.5|)})(1-0.46\cdot 10^{-15(|a-0.833|+|b-0.5|)})(1-0.5\cdot 10^{-18(|a-0.166|+|b-0.833|)}) \\ & \times(1-0.54\cdot 10^{-21(|a-0.5|+|b-0.833|)})(1-0.58^{-24(|a-0.833|+|b-0.833|)}) \end{aligned}$$

Here the variables *a* and *b* are assumed to vary in the range of [0, 1].

We use eight exponential functions to simulate eight local minima in the entire searching space. Each local minimum has different value and the smaller local minimum the larger decay constant in the exponential function. Therefore the function provides a test with more and more difficult to locate a local minimum with smaller value. These local minima are ordered in Fig. 2.6(b) in the order of #8, #7, #1, with the #8 denoting the global minimum.

(a)

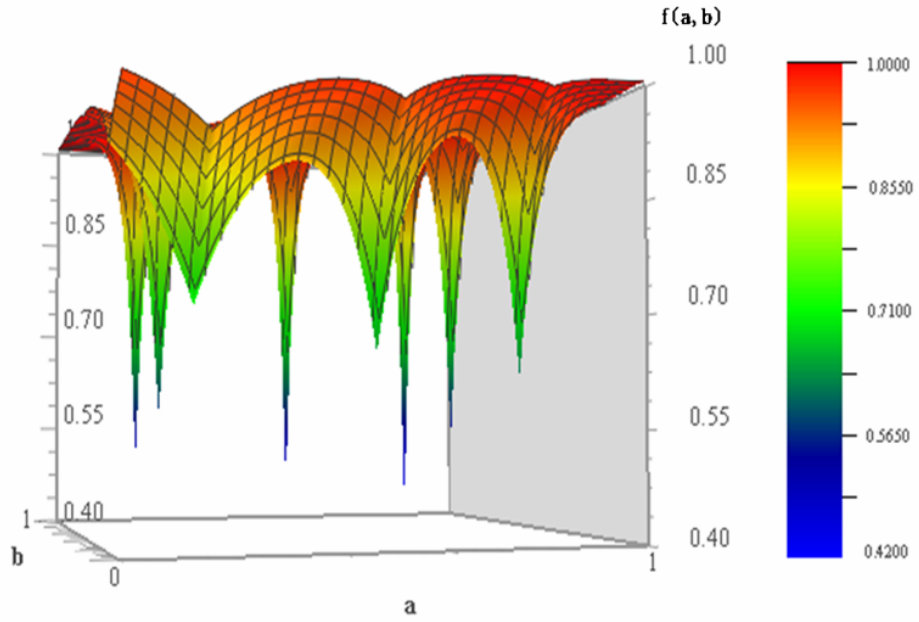

(b)

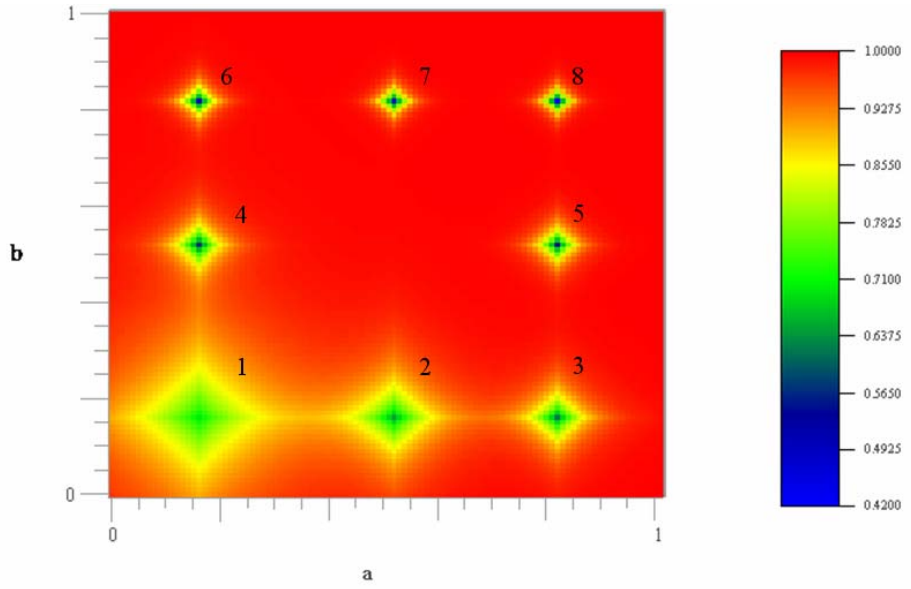

Fig. 2.6: (a) 3D and (b) contour plot of the testing function f(a, b).

The algorithms that are used in the optimization solvers are:

-Branch-and-bound global method (BB) + local search (LS)

-global adaptive random search (GARS) + local search (LS)

-multi-start based global random search (MS) + local search (LS)

For a fair comparison, we use the same iteration number k for each solver.

2.3.1 Branch-and-bound search method

Searching behavior of the branch-and-bound method is displayed in Fig. 2.7. Each searching region is subsequently split into 3 sub domains by the optimizer. After determining the lower and upper bounds of the three sub domains, the solver selects the most promising region and continues the domain splitting process. After this test run, the global minimum found by BB is the local minimum #6 shown in Fig. 2.6(b).

In Fig. 2.7, a disadvantage of the BB solver can be detected. In the beginning, the entire searching space is first split into 3 parts. But each domain is still too broad to precisely determine the upper and lower bounds. The BB optimizer arbitrarily chose the first domain for further search and therefore missed the other two local minima which in fact contain the correct global minimum.

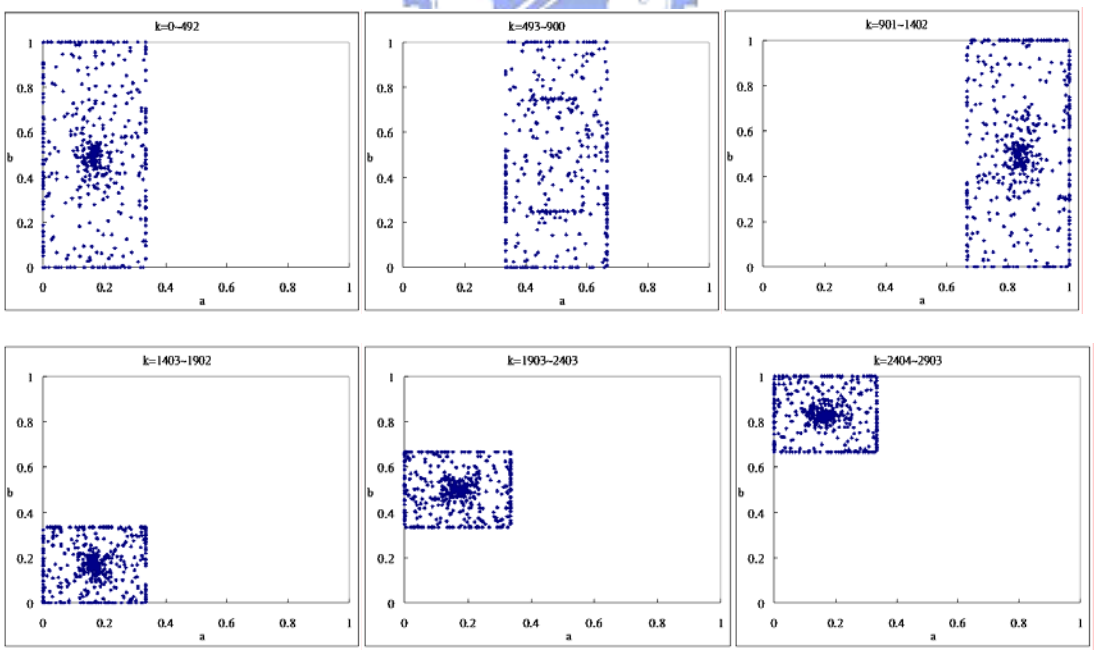

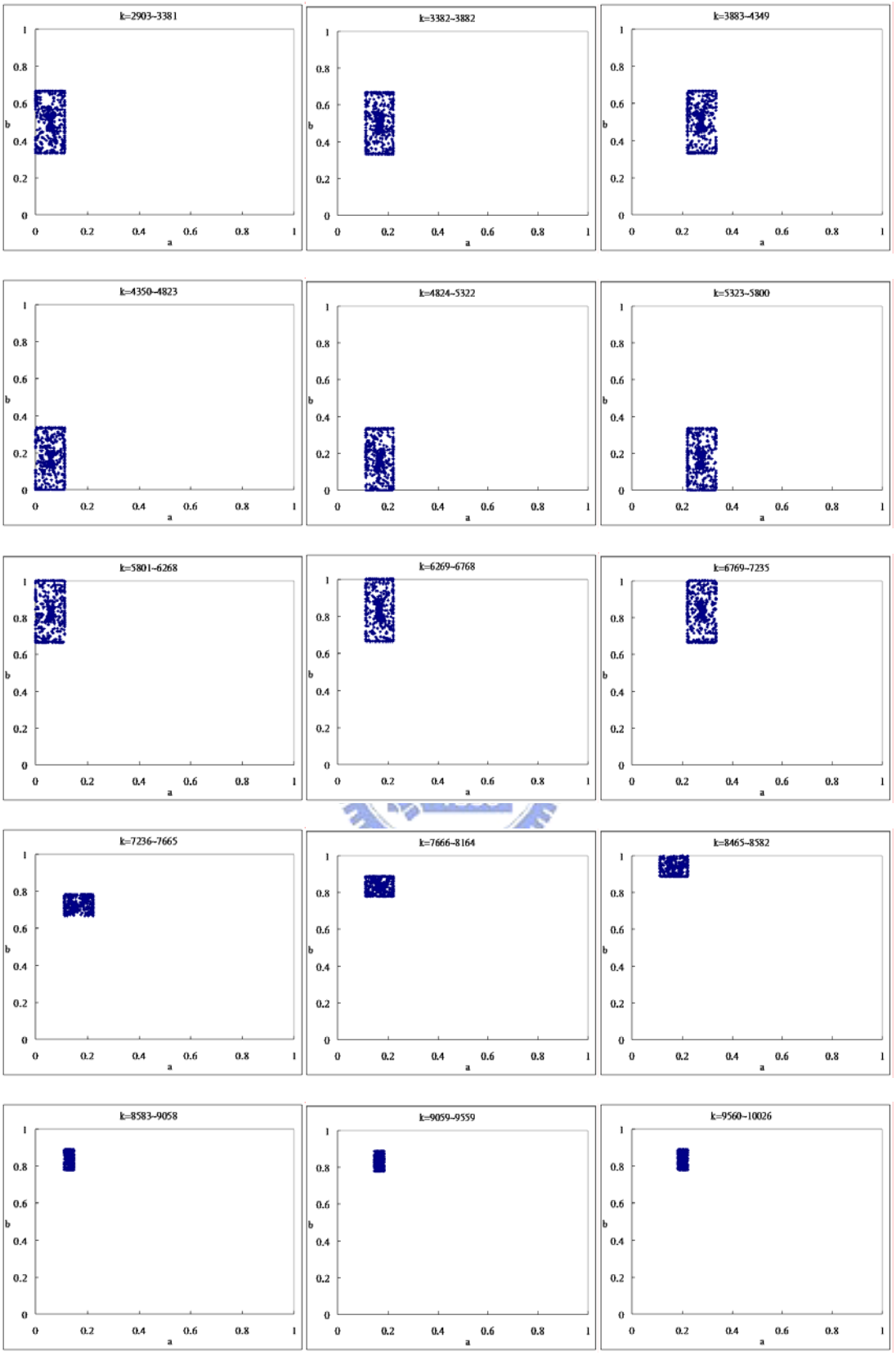
k=2903~3381
k=3382~3882
k=3883~4349
k=4350~4823
k=4824~5322
k=5323~5800
k=5801~6268
k=6269~6768
k=6769~7235
k=7236~7665
k=7666~8164
k=8465~8582
k=8583~9058
k=9059~9559
k=9560~10026
a
b

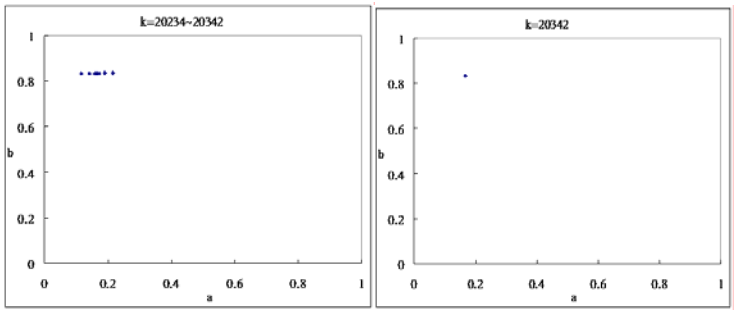

Fig. 2.7: Dynamic searching behavior of branch and bound method. We plot the sampling points in each searching space during iterations. Each searching region is subsequently split into 3 parts. Until iteration number k =20234, the solver changed to local search mode, and then stop at k= 20234.

2.3.2 Global adaptive random search

The search behavior of global adaptive random search is depicted in Fig. 2.8. This optimizer first reduces the searching region by limiting the range of the parameters *a* and *b*. However, at the beginning the local minimum #1 is so attractive for GARS that this optimizer misses the opportunity to find other local minima which are far separated from the local minimum #1. The optimizer finally stops at the local minimum #4.

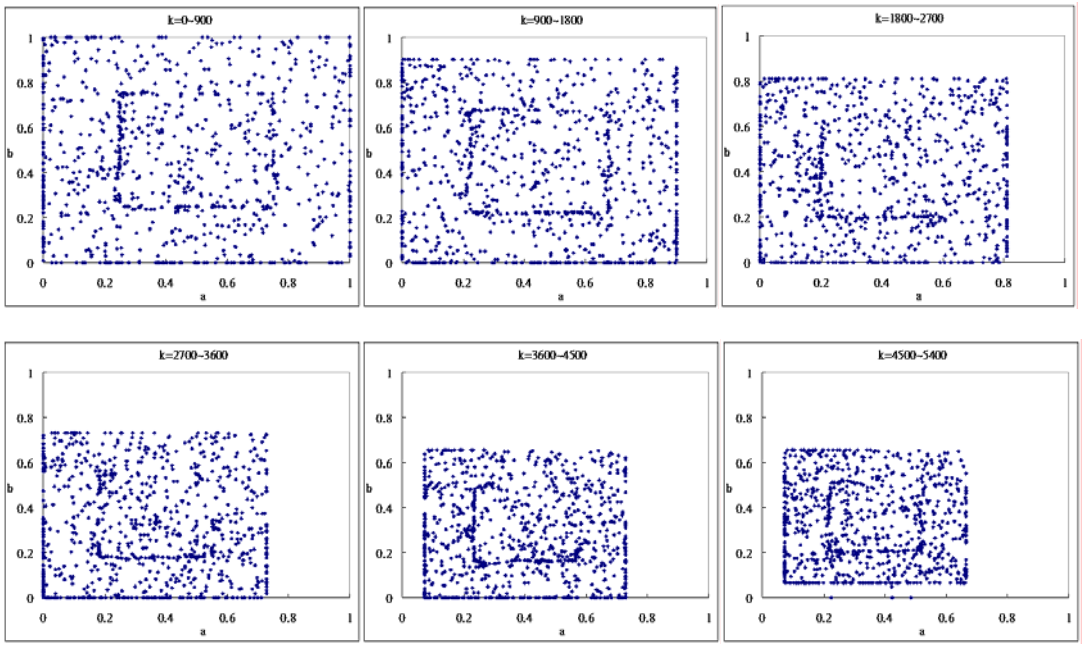

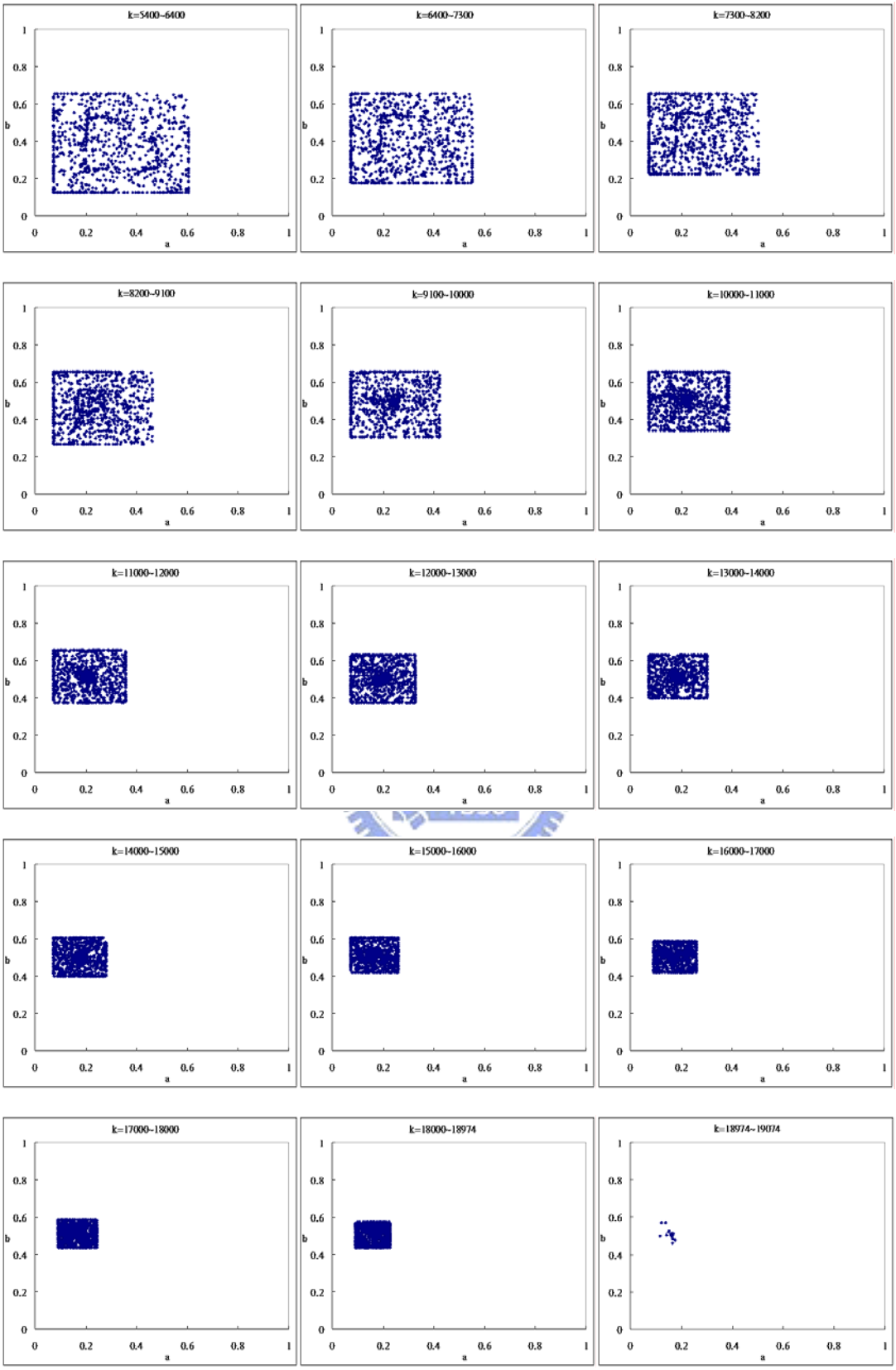
k=5400~6400
k=6400~7300
k=7300~8200
k=8200~9100
k=9100~10000
k=10000~11000
k=11000~12000
k=12000~13000
k=13000~14000
k=14000~15000
k=15000~16000
k=16000~17000
k=17000~18000
k=18000~18974
k=18974~19074
a
b

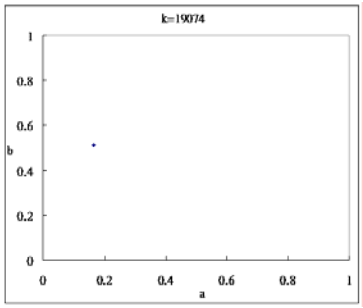

Fig. 2.8: Dynamic searching behavior of global adaptive random search. We plot the sampling points in each searching space during several iterations. The local search mode launches at k =18974~19074, and the optimizer stop at k =19074.

2.3.3 Multi-start-based global random search

We present the search behavior of multi-start based global random search in Fig. 2.9. The searching plot looks similar to GARS but MS-based optimization solver exhibits a more global nature in its search behavior. In fact, MS performs 15 times of global and local search during its entire searching process, and yields all of the eight local minima.

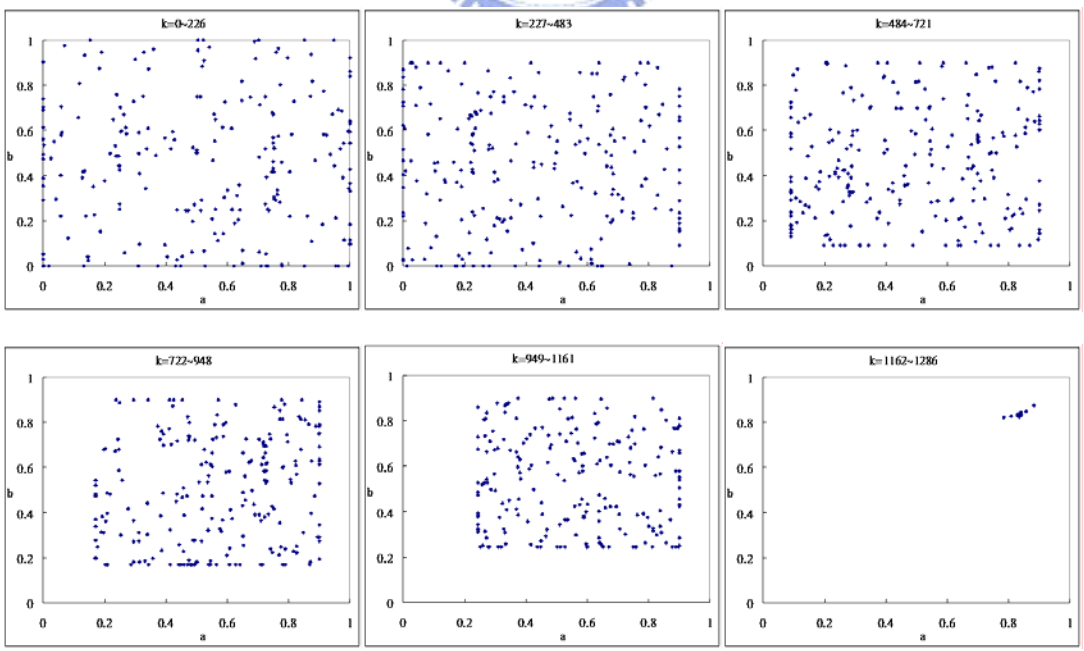

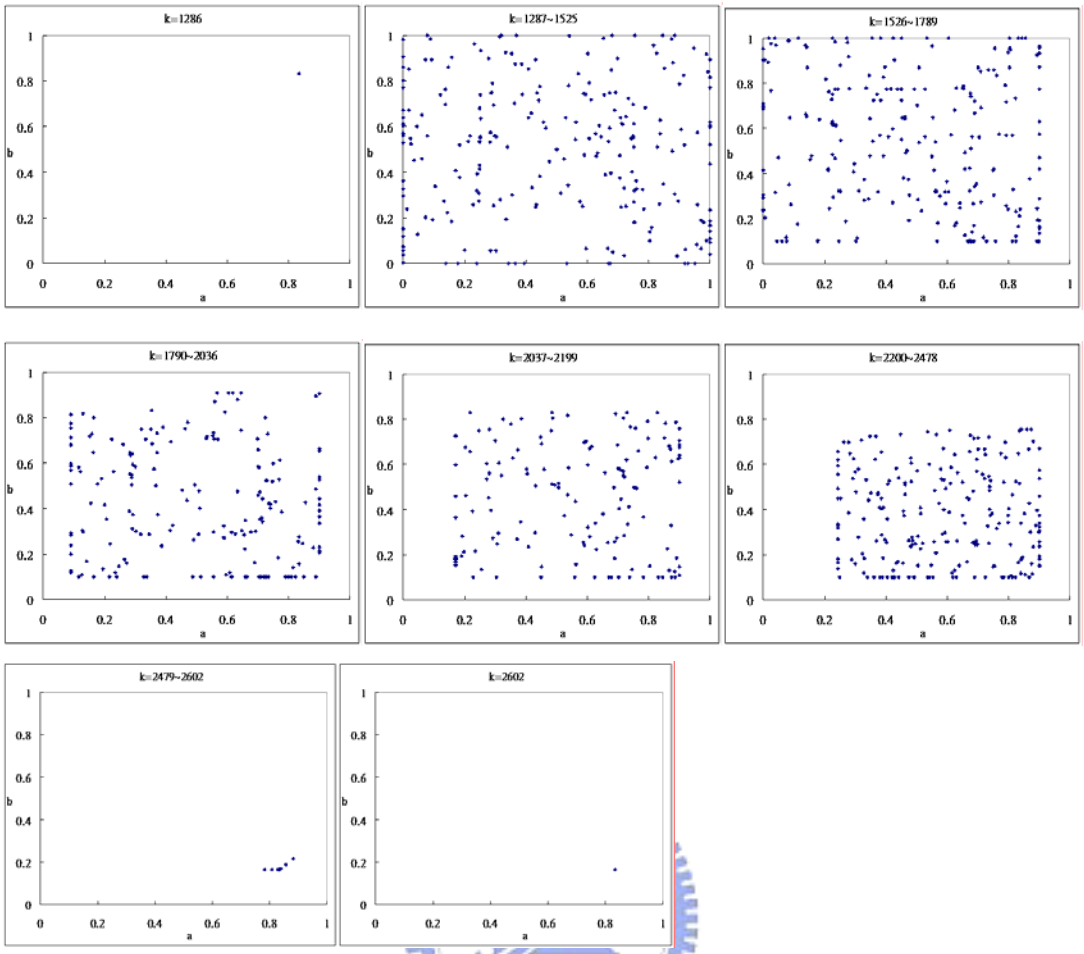

Fig. 2.9: Dynamic search behavior of multi-start random search. We plot the sampling points in each searching space during several iterations. Two local minima were found at k=1286 and 2602. After k= 2602, the optimizer continued to searching until k =20049 with a total 15 times of global search were performed. We only show the first two circles of the entire MS searching process.

2.3.4 Summary of This Section

Branch and bound is a systematical global optimization method. Although BB solver has a disadvantage, it succeeds in yielding smaller local minimum than that global adaptive random search can do. Global adaptive random search is less capable of handling functions with several competitive local minima and exhibits the worst performance among the three global optimizers tested in this study. Multi-start based random search can offer the correct solution. In addition, during the searching process,

MS solver provides other local minima, which may be of great help for yielding useful insight. For example, if we want to design an optical device with maximum transmittance. By using multi-start random search, we may be able to offer several designs with similar performance for further engineering evaluation. This allows us an extra freedom to choose a device structure with acceptable transmittance, but more compact and higher fabrication tolerance.

2.4 Benchmark Test Run with Fresnel Lens

We are planning to use the global optimization methods to yield optimal design of SOW devices. However, unlike to the test run shown in the previous section, in most cases the behaviors of SOW devices can not be properly depicted with a simple mathematical function. The SOW devices can only be described with a proper device simulator. In this section, we use a Fresnel lens as a benchmark of SOW device since its behavior can be described theoretically. To optimize the Fresnel lens, we define various cost functions in terms of the spot size at the focal point. We shall investigate the influence of the cost functions and compare the searching results and speeds with different global optimization algorithms.

2.4.1 Fresnel Lens

The device structure of a Fresnel lens is shown in Fig. 2.10. The device parameters are the thicknesses of the symmetric ring patterns (*i.e.* $d_1, d_2, d_3, d_4,$ and d_5). Note that the theoretical values of the thicknesses can be calculated with the equation reported in the literature [2]:

$$d(r) = d(0) - \frac{\sqrt{f^2 + r^2} - f}{n-1} \quad , \qquad (2\text{-}1)$$

where n denotes the refractive index of material, and f is focal length. The spot size SP can be calculated as

$$\begin{aligned} \mathrm{SP} &= < x^2 > - < x >^2 \\ < x^2 > &= \int x^2 \cdot E(x) \cdot dx \\ < x > &= \int x \cdot E(x) \cdot dx \end{aligned} \qquad (2\text{-}2)$$

where E is the magnitude of the incident optical field.

We try to obtain the best structure of the Fresnel lens with optimization. We first define the cost function as $f = \mathrm{SP}$ and then optimize the Fresnel lens with the multi-start random search. The iteration number is set to a large value of 9000. After optimization, the optimal structure (see Fig. 2.10) yields a spot size of 2.21 μm at the focal point and the optimal values of the device parameters are 0.82, 1.65, 2.55, 3.02, and 3.07 μm. By using Eq. (2-1), we calculate the optimal thicknesses to be 0.75, 1.72 2.45, 3.02, and 3.07. The optimal values of thicknesses agree well with the theoretical values, which ensure that the global optimization solver used here can yield the correct global optimal point.

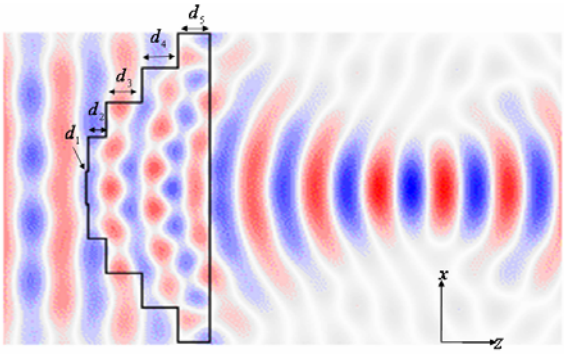

Fig. 2.10: Field distribution and schematic diagram of a Fresnel lens.

2.4.2 Influences of Cost Functions

In this section, we shall discuss the influences caused by different definitions of cost function with the three global optimization algorithms. To yield a clear

comparison, we first compare the searching efficiencies of the three algorithms by using the same cost function. We test the algorithms by increasing the iterations until the lowest number of iterations needed to produce the analytical result is found. The comparisons are presented in Table 2.1.

	BB	GARS	MS
iteration	1900	1400	2800

Table 2.1: Comparison of the lowest iteration number to produce the predicted result with the three searching algorithms.

Then we study the influences with different cost functions. Three different cost functions f_1 , f_2 and f_3 were used

$$\begin{aligned} f_1 &= \mathrm{SP} \\ f_2 &= -1/\mathrm{SP} \\ f_3 &= \mathrm{SP}^3 \end{aligned} \quad . \tag{2-2}$$

For the three cost functions, smaller spot size yields smaller function value. However, the second cost function is more sensitive in small spot size region and the third one is more sensitive in large spot size region.

We then determine the lowest iteration number needed to produce the analytic solution with branch and bound method and global adaptive random search. The third algorithm with multi-start adaptive random search is similar to that of the adaptive random search. So we neglect it in this comparison. The results are presented in Table 2.2. As it is shown, we can conclude that the definition of cost function does not lead to any difference in the optimal solution with global optimization solver, if and only if the cost function is a monotonic function of the device performance (SP).

	f_1	f_2	f_3
BB	1900	1900	1900
GARS	1400	1400	1400

Table 2.2: Lowest iteration number needed to produce the analytic solution with branch and bound method (BB) and global adaptive random search (GARS) by using the three different cost functions.

2.4.3 Summary of this section

Although global adaptive random search (GARS) is less capable of optimizing a function with multiple local minima (as example in Fig. 2-6), it becomes the most efficient solver with a device simulator. Multi-start based random search solver has the best performance among the three global optimizers; however it requires more iteration owing to its multi-start searching approach.

No difference in the optimal solution determined with global optimizer was detected with different cost functions. Thus in a practical design, we can simply use a cost function that can properly represent the desired response of device if the cost function is monotonic as a function of the device performance.

Chapter 3
Global Optimization Design of Sub-Wavelength Photonic Device

In this chapter, we combine a device simulator and optimizer to demonstrate optimal design of subwavelength photonic devices. The optimizer used has been depicted in detail in Chapter 2. The subwavelength photonic device simulator used is a fully vectorized electromagnetic simulation tool (CAMFR, http://camfr.sourceforge.net /docs/) based on eigenmode expansion method. In our studies, we first define a cost function and allow the optimizer to optimize the device design parameters based on the cost function.

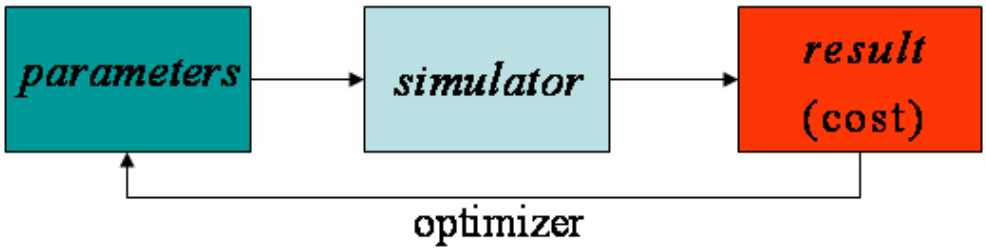

Fig.3.0.1: Flow chart of a global optimization design of subwavelength photonic devices.

Our motivations to use global optimizer to deduce the optimal device structure based on a predefined cost function of device performance are as follow.

- To yield better or similar performance with less consumption of fabrication resource;
- To verify the conjecture of device performance;
- By observing the optimized simulation results, we can construct a device model and

furthermore build a design rule.

To serve this purpose, four devices are to be presented in this chapter. They are: multimode interferometer (MMI)-based demultiplexer, aperiodic layered structure polarization beam splitter (PBS), nonlinear thickness taper, and LED-excited phosphor white light generator with omni-reflector.

3.1 Compact MMI for two-wavelength DeMux of Ethernet Passive Optical Network (PON) Application

3.1.1 Introduction

We can increase the information capacity of an optical fiber communication network by using different wavelengths of light. One of the core devices needed to achieve this goal is a multiplexer (Mux) or de-multiplexer (DeMux) to combine or divide the optical signals of different wavelengths. Some integrated-optic schemes have been proposed, which include conventional directional couplers, asymmetric Y-branching devices, and Mach-Zehnder interferometers [3] ~ [5]. However, these device structures exhibit some disadvantages of large device dimension or difficult to fabricate. In this section, a multimode interference device was chosen to demonstrate 1.3/1.5 μm DeMux function in view of the attractive features, such as easy to design and fabricate, low transmission loss, and large fabrication tolerance.

3.1.2 Theory

The operational principle of MMI device is based on its self-imaging

properties. *Self-imaging is a unique property of multimode waveguides by which an input field profile is reproduced in single or multiple images at periodic intervals along the propagation direction of the guide*. The local field distribution in a MMI device can be expressed as a superposition of the guided modes of the multimode waveguide involved:

$$\Psi(x,z)=\sum_{m} c_m \phi_m(x)\exp(j\frac{m(m+2)\pi}{3L_\pi}z), \qquad (3\text{-}1)$$

where ϕ_m is the modal field, c_m the excitation coefficient, β_m the propagation constant corresponding to the mode number m, and L_π is defined as the beat length of the two lowest order modes:

$$L_\pi \cong {4n_e W_e^2}/{3\lambda_0} \quad . \qquad (3\text{-}2)$$

Here n_e and W_e are the effective index and width of the waveguide. The detailed information about MMI can be referred to the reference [6].

From (3-1), we see that the total field distribution along the x direction is a periodic function of z. In other words, at the length of $L = q \cdot 3L_\pi$, a direct or mirrored image can be formed, where q can be an even or odd integer. Fig. 3.1.1 shows a periodic field distribution of a MMI structure, where the light is incident from the left side.

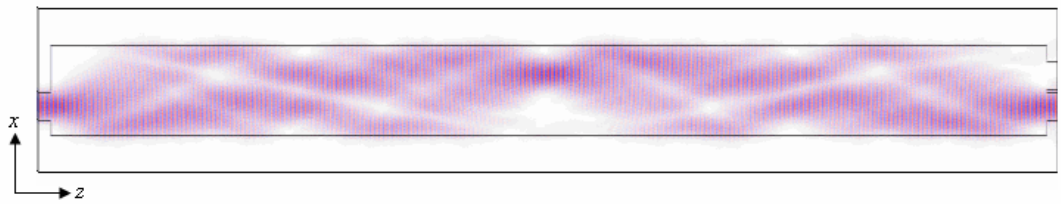

Fig. 3.1.1: A periodic field distribution in a MMI device. The light is incident from the left side of the device.

Eq. (3-2) shows that L_π is a function of λ_0. Thus, we can implement a wavelength-resolving power into a MMI and make the MMI behave like a demultiplexer by adjusting the device length to be $3L_\pi$ for one wavelength and $6L_\pi$ for the other. However, the total length of the device will be very long [7] ~ [8]. For example, we typically obtain a total length of about 200 μm for SiON with W=10 μm at λ=1.3 μm. Some approaches have been proposed to shorten the device length, which include a combination of MMI and a chirped grating [9]. In this way, the total device length was shown to be reduced to about 600 μm. However the insertion loss of the device is also significantly increased. Note that in Fig. 3.2, double images are also formed at the distances of $3L_\pi/2$ and $9L_\pi/2$. Thus, MMI can also be used as a 3-dB power splitter.

3.1.3 Optimal Design of MMI DeMux

To shorten the device length of MMI DeMux, we propose a device configuration showed in Fig. 3.1.2. Optical signals of λ=1.3 μm and 1.5 μm are injected into the device from the left side. We like to steer the optical signals to different output port of the device based on their wavelengths. We divide the MMI structure into three regions: section 1, section 2, and section 3, with the length of L1, L2, and L3, respectively. The design parameters are L1, L2, L3, w_1, w_2, w_p, t, and W_{MMI}. We use global optimization solver to adjust these parameters based on the following cost function

$$\text{cost function} = \left(\frac{P_1^{1.5}}{P_1^{1.3}}\right)+\left(\frac{P_2^{1.3}}{P_2^{1.5}}\right)+\left(\frac{1}{P_1^{1.3}}\right)+\left(\frac{1}{P_2^{1.5}}\right). \quad (3\text{-}3)$$

The cost function is designed to yield a high contrast and low insertion loss of the MMI DeMux. Contrast and insertion loss are defined to be $10\cdot\log(P_{o,r}/P_{o,w})$ and $10\cdot\log(P_{o,r}/P_i)$, respectively, where P_i denotes the intensity in the input port, and

$P_{o,r}$ and $P_{o,w}$ represent the fractional powers appearing at the right and wrong output ports of the device.

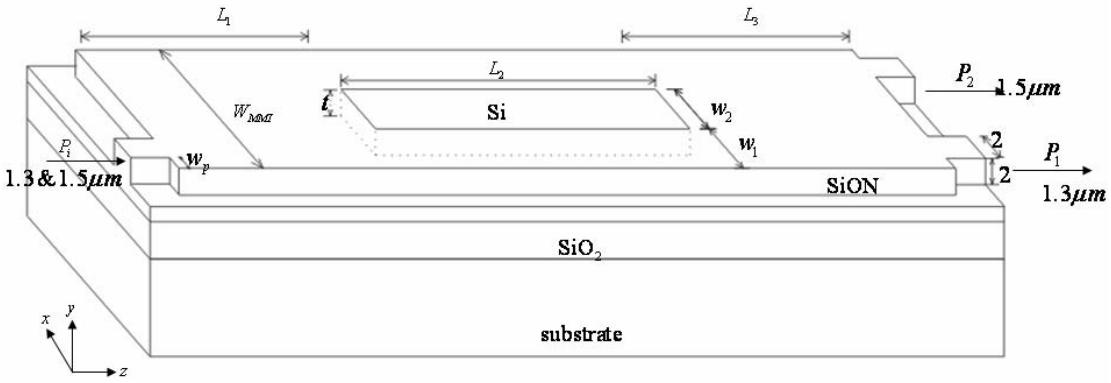

Fig. 3.1.2: Schematic showing the MMI device configuration of our design

After optimizing the device performance, we obtain an optimal device with the structure shown in Fig. 3.1.3 and the parameters are also listed in Table3.1. The resulting contrast is 15.0 dB at $\lambda = 1.3\mu m$ and 17.2 dB at $\lambda = 1.5\mu m$ with the corresponding insertion losses being 0.56 dB and 0.51dB, respectively.

(a)

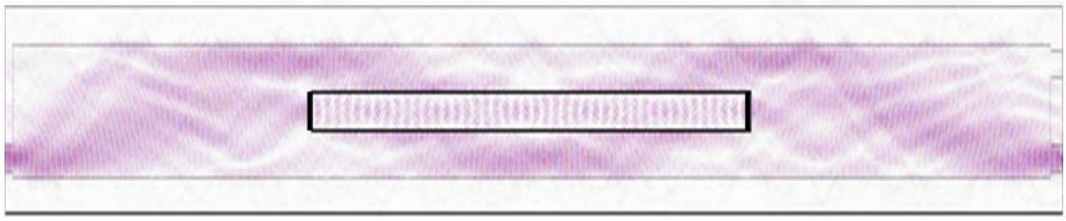

(b)

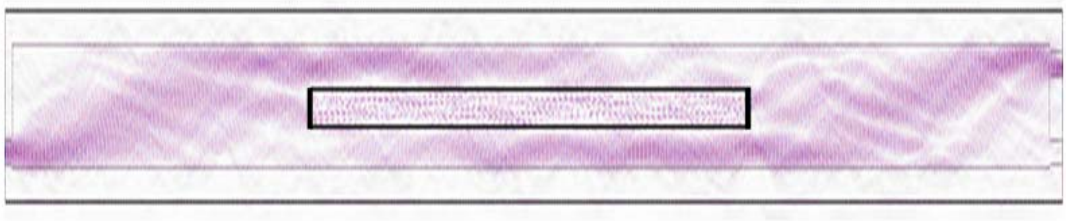

Fig. 3.1.3: Field distribution of our optimal device at wavelength of (a) 1.3 μm, and (b) 1.5 μm.

L_1=89.7μm	L_2=132.3μm	L_3=89.8μm
w_1=3.2μm	w_2=2.87μm	w_p=0.44μm
t=1.44μm	W_{MMI}=9.27μm	

Table 3.1: List of the optimized parameters for MMI DeMux.

3.1.4 Discussion

In Fig. 3.1.3, triple images of the field distribution appear to occur at a propagation distance of L1 for both two wavelengths. Therefore behind the section 1, we introduce a rectangular region with different effective index into the central part of section 2. We can consider section 2 as three coupled channel waveguides. The three beam images formed at the end of section 1 now enter into the three coupled waveguides. The guided power in each waveguide of the section 2 will couple with each other, and the coupling length at the two wavelengths is different. From Fig. 3.1.3, we can see that the length L2 of section 2 is equal to the coupling length at 1.5 μm and twice the coupling length of 1.3 μm. So the guided power in the upper waveguide can be transfer to the lower waveguide then back to the upper waveguide for light with λ=1.3 μm. For light with λ= 1.5 μm, the guided power in its initial waveguide will transfer to the other waveguide. In other words, the field distribution of 1.5 μm in the beginning of section 2 will be inversed in the end of section 2. The propagation function of section 3 is just to reverse that in section 1, so the light appears at the device output will be focused on the lower output port for the light with the wavelength of 1.3 μm. Because the field distribution of 1.5 μm is reversed at the end of section 2, the distribution of the guided power will be focused on the upper output port and therefore two optical signals with different wavelengths are separated.

Based on the conjecture on the device operation principle, we can surmise that the length of L1 and L3 must be very similar. The optimized values of L1 and L3

indeed were found to be L1=89.7 μm and L3=89.8 μm. The field profile in the section 1 of our optimized device is presented in Fig. 3.1.4. We can clearly see that the incident light was separated into 3 beams after propagating for a length of L1. The triply splitting length shall be equal to $L_\pi/2$, which is found to be 90 μm for λ=1.3 μm and 78.3 μm for the wavelength of 1.5 μm. Note that the three beam images persist for a certain length. So the length of L1 is not necessary to be restricted to $L_\pi/2$. This leads to a higher design tolerance for our design.

(a)

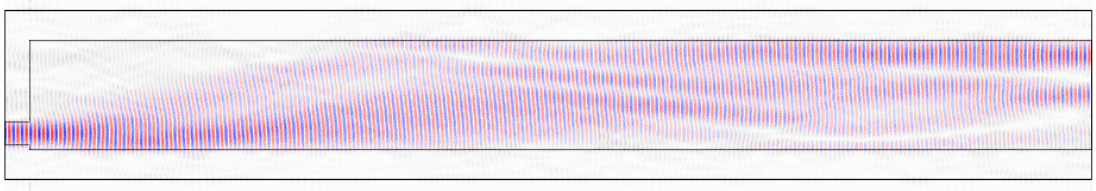

(b)

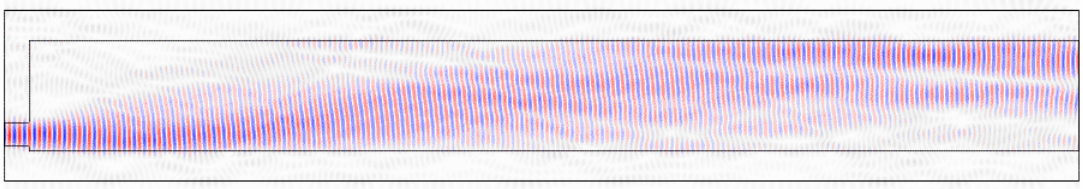

Fig.3.1.4: Field profile in section 1 of our device with wavelength of (a) 1.3 μm, and (b) 1.5 μm.

For a MMI device, input field profile can form a multiple images at periodic distances along the propagation direction of the device. The location of the multiple images can be expressed as:

$$L = \frac{p}{N}(3L_\pi), \qquad (3\text{-}4)$$

where N and p are integers with N≥1 and p≥0. N denotes the number of images, and p indicates the occurrence number of the N-images. We can therefore expand the field distribution profile $\Psi_{in}(x)$ at the input of a MMI ($0 < x < W_{MMI}$) in terms of periodic

Fourier components:

$$\Psi_{in}(x) = \sum_{n=-\infty}^{\infty} (\Psi_{z=0}(x+2nW) - \Psi_{z=0}(-x+2nW)) \qquad (3\text{-}5)$$

The field profile at the positions of multiple images can be written as:

$$\Psi(x) = \frac{1}{C}\sum_{q=0}^{N-1} \Psi_{in}(x - x_q)\exp(j\varphi_q), \qquad (3\text{-}6)$$

$$\text{where} \quad x_q = p(2q-N)\frac{W_{MMI}}{N} \quad \text{and} \qquad (3\text{-}7)$$

$$\varphi_q = p(N-q)\frac{q\pi}{N} \quad . \qquad (3\text{-}8)$$

C is a complex normalization constant. The detailed derivation can be found in the reference [10]. The location of $L_\pi/2$ is the position that the field distribution produces six image spots. But the total width of our device is not wide enough, so the six images combine to form three beam images with different intensity. By using Eqs. (3-5) ~ (3-8), we can calculate the magnitude of field at the position of z= $L_\pi/2$ and the result is shown in Fig. 3.1.5. If the input port is located inside the lower 1/3 of the MMI device, the incident light can be separated into 3 beams after propagating for a distance of $L_\pi/2$. That is w_p+2 must be smaller than $W_{MMI}/3$, where w_p is the width of the input port.

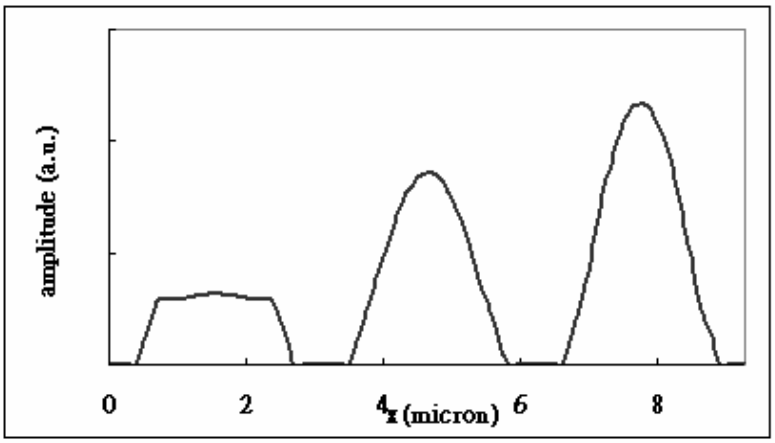

Fig. 3.1.5: Transverse field distribution profile of our device at the position of z $= L_\pi/2$.

Field distribution in section 2 of our device is shown in Fig. 3.1.6. The coupling lengths of the upper and lower waveguides are calculated to be 144 μm and 134 μm for the signal wavelengths 1.3 and 1.5 μm. The optimized L2 is 132 μm. So most guided power at the wavelength of 1.5 μm in one waveguide is transferred to another waveguide. For the wavelength of 1.3 μm, most guided power remains in its original waveguide after propagating through section 2.

(a)

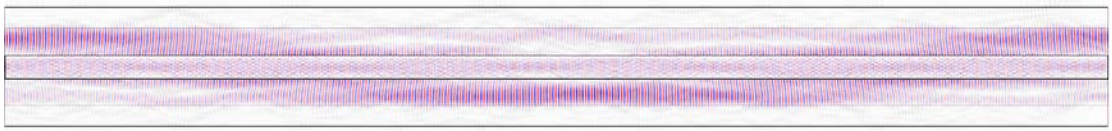

(b)

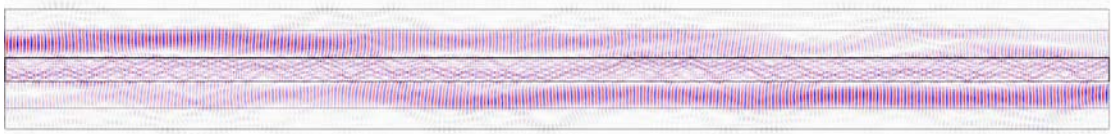

Fig. 3.1.6: Field distribution in section 2 of our optimized device with the wavelength of (a) 1.3 μm and (b) 1.5 μm.

Now we discuss the fabrication tolerance of our device. Fabrication tolerance refers to the impact of the geometric variations on device performance, and it is important for the practical fabrication process. L_2 and w_2 are the most two sensitive parameters in our design. Performance of the MMI demultiplexer as a function of the length of L_2 and w_2 are shown in Fig.3.1.7 and Fig.3.1.8. The thickness of w_2 has a bad fabrication tolerance and tolerates only several nanometers of distortion.

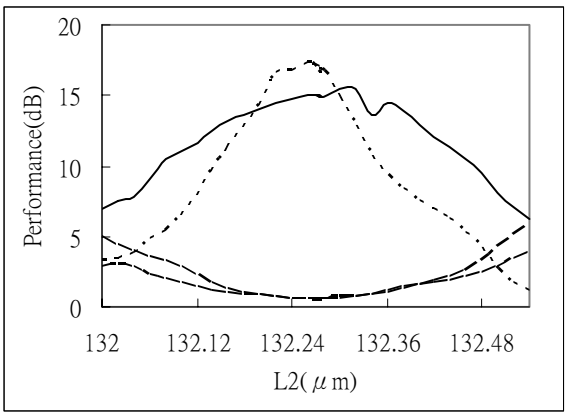

Fig. 3.1.7: Performance of the MMI demultiplexer as a function of the length of section 2 with other parameters fixed.

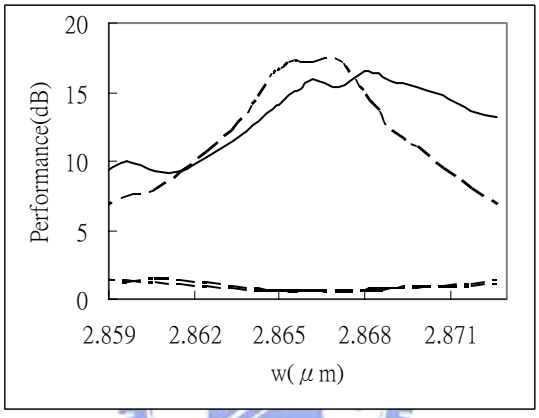

Fig. 3.1.8: Performance of the MMI demultiplexer as a function of the width of w_2 with other parameters fixed.

3.1.5 Summary of This Section

A compact 1.3/1.5 μm wavelength multiplexer/demultiplexer based on multimode interference was designed. The device length can be reduced by using optical coupling effect by introducing a rectangular region in section 2. By comparison to a traditional MMI device, the device length of our design can be greatly reduced by comparing with a tradition MMI, which is made of the same material but without the section 2.

Comparison	λ (μm)	contrast	loss	Total length
Our Design	1.3	15.0 dB	0.56 dB	311.7μm
	1.5	17.2 dB	0.51 dB	
Traditional MMI	1.3	18.6 dB	0.32 dB	1833μm
	1.5	17.2 dB	0.29 dB	

Table 3.2: Comparison between a traditional two-wavelength MMI DeMux and our new design.

Two reasons can be offered to explain why our design can have a shorter device length:

- L1 and L3 are equal to about $L_\pi/2$, which is 1/12 of the period of a conventional MMI structure.
- The coupling length in section 2 is much smaller than the period of a conventional MMI structure.

In this section, we demonstrate a unique opportunity yielding from the application of global optimization solver: By analyzing the optimized structure, an idea can be inspired for a new design of MMI DeMux. We can therefore discover a new device structure which meets the desired functionality of two-wavelength de-multiplex ion

3.2 Aperiodic Layered Grating Structure for Broadband Polarization Beam Splitting

3.2.1 Introduction

Polarization beam splitters (PBS) are an indispensable device for numerous applications, ranging from magneto-optical data storage in optical information processing, optical switching in optical communication to polarization-based imaging systems. Conventional PBS devices, such as Wollaston prism and PBS cube, are either bulky and heavy or only working in a narrow wavelength range. Subwavelength grating (SWG) is a new way to avoid these disadvantages [12]~[14]. The characteristics of subwavelength devices, such as compact and light weight, are advantageous to the miniaturization and integration of optical systems.

However, performance of periodic multi-layered structure, such as distributed Bragg reflectors, is sensitive to wavelength, incident angle, and polarization of light. PBSs based on subwavelength gratings with periodic layered structure [12] are also limited to a narrow wavelength range. In this section, we report a new design of a subwavelength grating PBS which can work in a broad wavelength range. The design uses an aperiodic layered structure.

3.2.2 Theory

PBS functionality with a subwavelength grating structure is originated from the form birefringence effect [11]. Although the conventional birefringent properties of a material come from the anisotropic electronic distribution of the material, optical birefringence may also be generated from an anisotropic geometry at a scale much

larger than the composing unit. In other words, optical birefringence can be artificially generated from an ordered arrangement of optically isotropic materials, which is now called *form birefringence* (see Fig. 3.2.1).

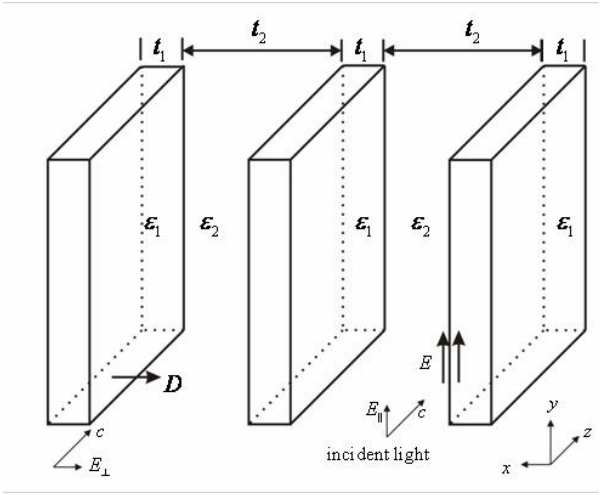

Fig. 3.2.1: Form birefringence of thin parallel plates with t_1 and t_2 smaller than the wavelength of light.

Assuming that a plane wave is incident on a structure shown in Fig. 3.8 and its electric vector is perpendicular to the plates. According to the boundary condition, the normal component of the electric displacement D must be continuous across the interface. Thus, if E_1 and E_2 are the electric fields in medium 1 and 2, and $\bar{E}$ denotes the averaged field over the total volume

$$\bar{E} = \frac{t_1 E_1 + t_2 E_2}{t_1 + t_2} = \frac{t_1 \dfrac{D}{\varepsilon_1} + t_2 \dfrac{D}{\varepsilon_2}}{t_1 + t_2}, \tag{3-9}$$

the effective dielectric constant $\varepsilon_\perp$ is, therefore,

$$\varepsilon_\perp = \frac{D}{\bar{E}} = \frac{(t_1 + t_2)\varepsilon_1 \varepsilon_2}{t_1 \varepsilon_2 + t_2 \varepsilon_1} \quad . \tag{3-10}$$

For the incident light with electric vector parallel to the plates, the boundary condition becomes: the tangential component of the electric vector is continuous across the interface. In this case, the electric field will have the same value E no matter inside or

outside the material. We can finally obtain an effective dielectric constant

$$\varepsilon_{\square} = \frac{\bar{D}}{E} = \frac{t_1\varepsilon_1 + t_2\varepsilon_2}{t_1 + t_2} \tag{3-11}$$

where $\bar{D}$ is the averaged electric displacement.

Fig. 3.2.2 shows a schematic diagram of the subwavelength grating-based PBS. From Eqs. (3-10) and (3-11), we can calculate the effective refractive index $n_{\perp}$ and $n_{\square}$ for both polarization directions. Since the reflectance and transmittance is dependent on index of refraction, we can modify the reflectivity and the reflectance bandwidth by using materials with larger refractive index contrast. When the effective index ratio between the two materials for TE polarization is larger than that of TM, TE polarization will experience a stronger reflection. By this way, we can emulate a PBS function. By comparing the coordinates systems shown in Fig. 3.2.1 and Fig. 3.2.2, we found that $n_{\perp} = n_{TM}$ and $n_{\square} = n_{TE}$.

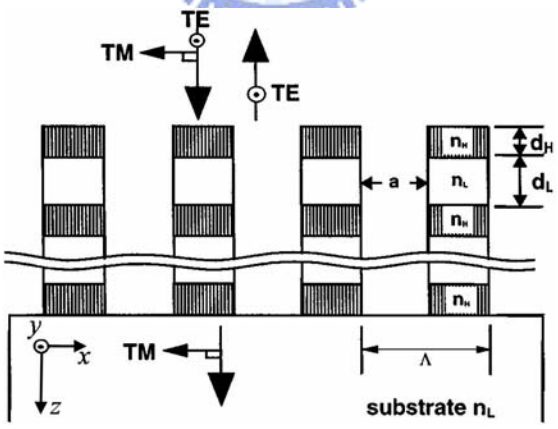

Fig. 3.2.2: Schematic diagram of a subwavelength grating-based PBS

3.2.3 Device Design and Optimization

We use SiO_2 and Si, which have a refractive index of 1.45 and 3.51, respectively at the wavelength of 1.3 μm, as the low/high index materials for the

multilayer structures in view of their fabrication compatibility and low absorption in near-infrared region. We choose $a=\Lambda/2$, and the number of layers is 15. We consider one pair of SiO_2 and Si as a unit with a pair thickness of d_k (k=1, 2, 15). Then, we use global optimization to optimize these design parameters, which comprise of the thickness of each layer d_k, grating period Λ, and the thickness ratio of Si and SiO_2 (*i.e.* ratio=d_H/d_L). The pair thickness is defined to be $d_k= d_{H,k}+d_{L,k}$.

From Eqs. (3-10) and (3-11), we first can calculate the effective refractive indices $n_{TM}=1.36$, $n_{TE}=2.6$ for Si layer and $n_{TM}=1.16$, $n_{TE}=1.25$ for SiO_2 layer. The effective index ratio of two materials is 2.08 for TE polarization and 1.17 for TM. TE polarization typically has a higher reflectivity. We design our PBS to have a high reflectivity for TE and high transmittance for TM. Therefore the cost function for our global optimizer can be defined as:

$$\text{cost function} = \sum_i [(T_i^{TE}/T_i^{TM})+(R_i^{TM}/R_i^{TE})], \qquad (3\text{-}11)$$

where *i* represents different wavelengths of the incident light. We use five discrete wavelengths at 1.0, 1.1, 1.3, 1.5, and 1.7 μm for optimization. By minimizing the cost function, we can get a PBS with high extinction ratio and broad range of operation wavelength.

After optimizing the device parameters, we obtain an optimal device structure (shown in Fig. 3.2.3) and the optimized parameters are listed in Table 3.3. For an incident light of 1.3 μm, the transmittance of TM polarization is 97.3%, and the reflectance of TE polarization is 99.8%.

layer thickness =(0.09, 0.29, 0.27, 0.37, 0.34, 0.2, 0.21, 0.29, 0.45, 0.37, 0.5, 0.2, 0.32, 0.2, 0.45) μm Λ=0.3μm ratio=0.49

Table 3.3: List of the optimized parameters for aperiodic sub wavelength grating PBS.

Fig. 3.2.4 also shows the performance of our device with incident light of different wavelength from 1.0 to 1.7 μm. We compare the performance of our aperiodic device structure to that with periodic layer thickness. We can clearly see that the operation bandwidth of the periodic layered structure is much narrower than that of aperiodic structure.

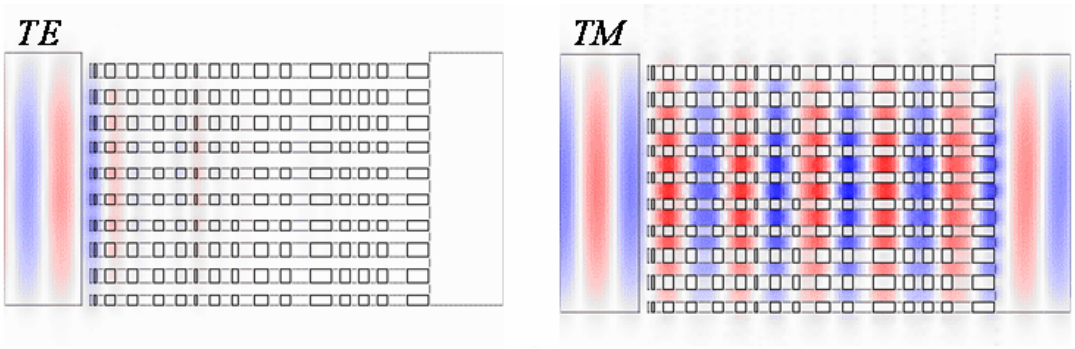

Fig. 3.2.3: Field distribution in our PBS design at wavelength of 1.3 μm. The transmittance of TM is 97.3%, and the reflectance of TE polarization is 99.8%.

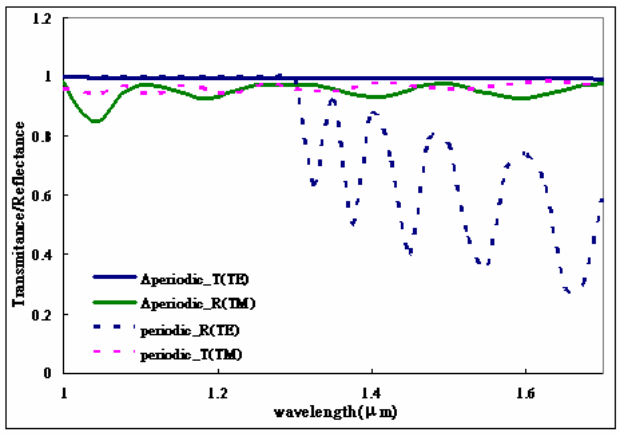

Fig. 3.2.4: Comparison of the performances of our PBS design and a device with periodic layered structure. The wavelength of incident light is assumed to vary from 1.0 to 1.7 μm.

3.2.4 Discussion

Why our design can meet the performance requirement? By examining the distribution of layer thicknesses determined by global optimization, we can see that the layer thicknesses of our design can be separated in several groups, {0.29, 0.37, and 0.45 μm}. We therefore surmise that the broadband PBS function is generated by combining several periodic layered structures with a narrower operation bandwidth.

To achieve a broadband operation with a stacked periodic layered structure, the transmittance of TM polarization of each periodic layered segment shall be near to 1. The reflectance of TE polarization of each periodic layered segment must be complementary for each other to yield high reflectance in a broad spectral range. The reflectance spectra of the three periodic layered segments with a pair thickness of 0.29, 0.37, and 0.45 μm, are presented in Fig.3.2.5. The high reflectance range for each segment does not cover the entire spectral region from 0.9 to 1.7 μm, but the three periodic layered segments stacked together can yield high reflectance from 0.9 to 1.7 μm.

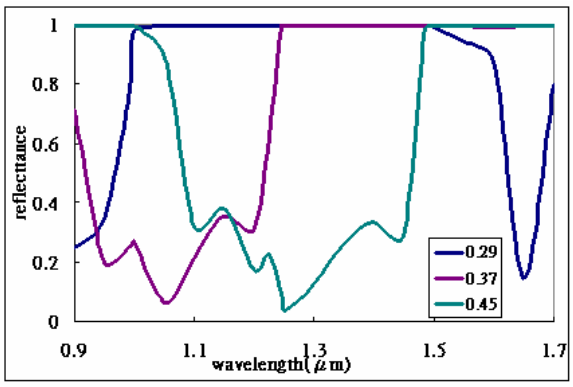

Fig. 3.2.5: Reflectance spectra of periodic layered structures with a pair thickness of 0.29, 0.37, and 0.45 μm, respectively. The high reflectance ranges for the three structures stacked together can add to form a broad range of operation from 0.9 to 1.7 μm.

Our PBS has high fabrication tolerance as shown in Fig.3.26. We arbitrarily chose one layer (the thickness is 295nm) to change its thickness and the distortion means the thickness difference. The incident light is in the wavelength of 1.3 μm.

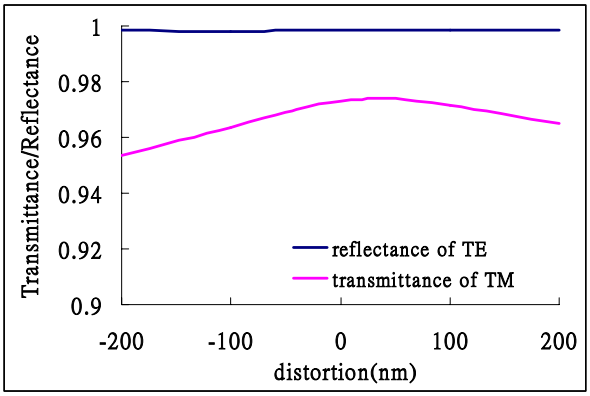

Fig. 3.2.6: Fabrication tolerance of our device.

3.2.5 Summary

We successfully design an aperiodic layered structure with a subwavelength grating for providing PBS function in broad spectral range. The designed performance is shown in Fig. 3.2.4. The pair thicknesses of the aperiodic layered structure are determined with global optimization solver by using a specified cost function. The operation bandwidth of our device is broader than that with periodic layered structure (Fig. 3.2.5). Global optimization technique is not only a useful tool to help us discovering the optimal device parameters, but also a unique technique to inspire our insight into the model of the optimized device.

By examining the optimized device structure discovered by global optimization solver, we understand that the broadband functionality of the aperiodic layered structure could be originated from a stack of at least 3 periodic layered segments with different operation wavelengths.

3.3 Compact Z-taping Structure for Low Loss Input/Output Light Coupling into Photonic Integrated Circuit Chips with High Index Contrast

3.3.1 Introduction

In an integrated optic circuit, we usually need a taper structure to couple photonic devices with different scales of guiding region. Tapered waveguides can also be used for input/output coupling to single mode fibers[15] and for semiconductor laser amplifier applications[16].

For a linear tapered waveguide, we usually need a long length to decrease the optical loss. In order to reduce the taper length and increase the efficiency, a design of a parabolic tapered waveguide had been previously reported [17]. However, the design can only ensure a low loss operation of a symmetric tapered waveguide. For a vertical taper, it is also difficult to fabricate a symmetric structure.

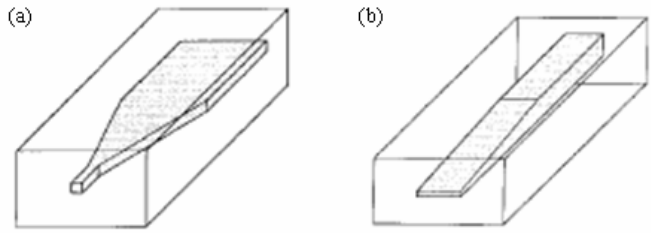

Fig.3.3.1: Schematic diagram showing (a) a lateral taper and (b) a vertical taper.

In this section, we try to design a vertical taper for the purpose of an efficient coupling between a single mode high-index waveguide and a single mode fiber.

However, other than a traditional linear vertical taper, our design controls the taper profile to achieve higher coupling efficiency and shorter device length.

In order to increase the coupling efficiency, we have to reduce the mode mismatch between waveguide and single-mode fiber. Mode mismatch means the mismatch of the field profile between the incident field and target guiding mode. There are two ways to reduce the mode mismatch: Firstly, we can use a mode transformer to transform the mode profile between fiber and waveguide. For the second way, we can use a nanometer-size waveguide as shown in Fig. 3.3.2. The field

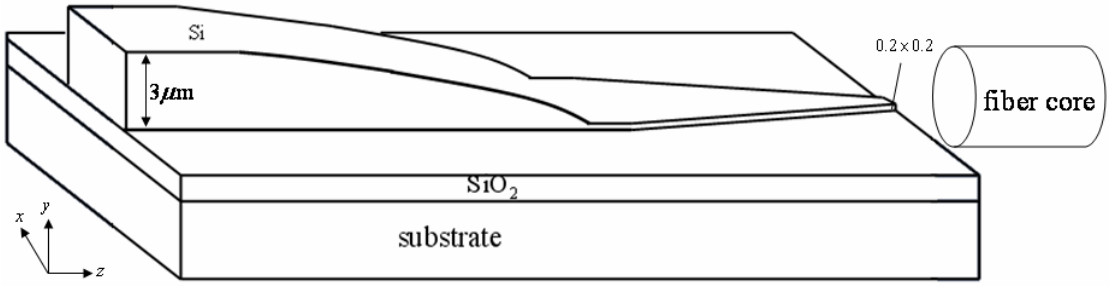

Fig. 3.3.2: Coupling between single mode fibers and a waveguide.

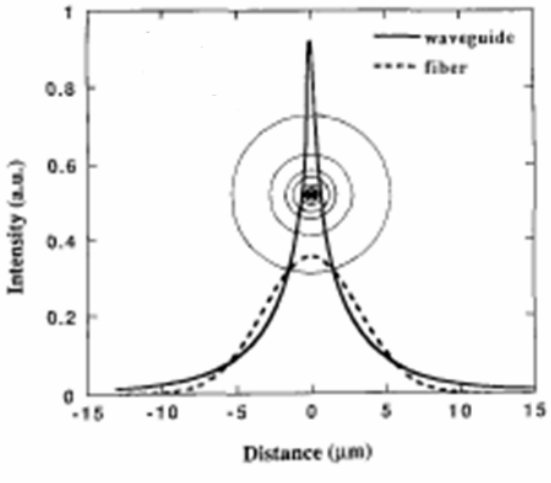

Fig. 3.3.3: Mode field profiles of a nanometer-size waveguide and a single mode fiber. The field profile expansion from the nanometer-size waveguide produces a large mode profile which is similar to that of a single mode fiber.

profile expansion from the nanometer-size waveguide produces a mode field distribution similar to a single mode fiber (see Fig. 3.3.3). The mode mismatch can be reduced in this way and the coupling efficiency will be increased.

3.3.2 Design and Optimization

We follow the second mode-matching method described in 3.3.1 to design a vertical tapered waveguide. The thickness of the guiding layer is 3 μm initially and is reduced to 0.2 μm at the end of the taper. The vertical taper region is shown in Fig.3.3.2. An optimized vertical taper profile, which can be fabricated by gray-level mask and dry etching techniques, can be properly depicted with a third-order polynomial. The optimized profile can reduce the taper length while improve the coupling efficiency. We express the third-order polynomial function as

$$z = ah^3 + bh^2 + ch + d\,, \qquad (3\text{-}12)$$

where h =h(z) denotes the thickness of the taper at position z and *a*, *b*, *c*, *d* are four coefficients. In order to obtain the optimized structure with minimum propagation loss, we use a global optimization solver to adjust these coefficients. Since the initial and final thicknesses are fixed to be 3 and 0.2 μm, respectively, only 3 parameters are left to be adjusted independently.

After optimizing the three parameters, we obtain a third-order polynomial taper with a profile being presented in Fig.3.3.4 with a=0.524, b=0.172, c=1.399 and d=-0.291. For an incident light beam at 1.3, the optimal transmittance is 91.9% with a taper length as short as 19.6 μm.

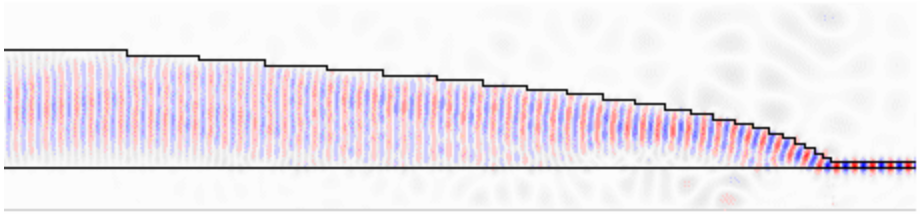

Fig. 3.3.4: Vertical taper with a third-order polynomial profile obtained by global optimization solver to maximize the transmission efficiency. The transmittance is 91.9% and the taper length is only 19.6 μm.

3.3.3 Discussion

For comparison, we also optimize a tapered waveguide with a linear profile (see Fig.3.3.5). For a proper comparison, the length of the linear taper is set to no longer than 30 μm. After optimization, we found the maximum transmittance to be 81.5% and the taper length 29.4 μm. Apparently, the transmittance of the linear taper is lower and the device length is longer than the third-order polynomial taper.

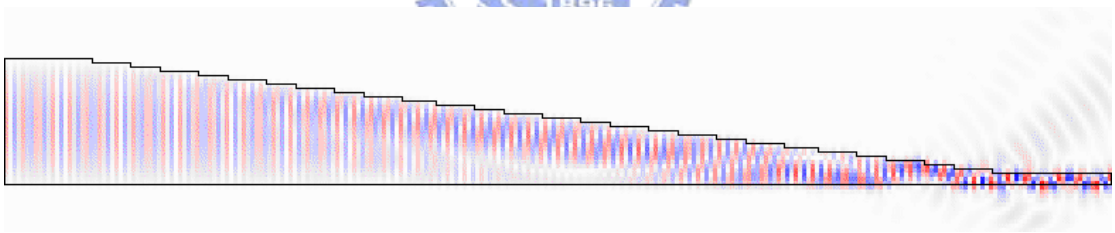

Fig. 3.3.5: Linear tapered waveguide with transmittance of 81.5% and taper length of 29.4 μm.

Form the field distribution plot shown in Fig.3.3.5, the performance of the linear taper can be modeled as plane wave incidents from the left side as shown in Fig.3.3.6. The incident angle of the ray becomes smaller and smaller at the upper and lower interface, and finally the incident angle becomes even smaller than the critical angle of total internal reflection and optical power is no longer confined beyond this position. In order to prevent the optical loss, we need to lower the slope of the linear tapered structure and causes an increase of the device length.

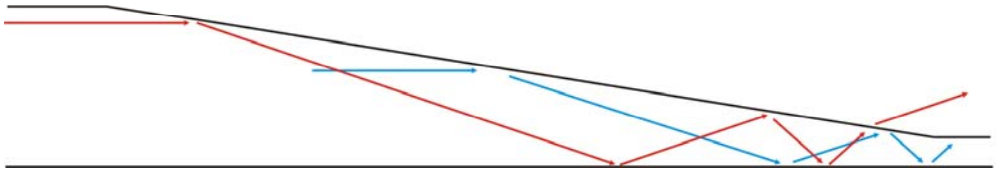

Fig. 3.3.6: Optical ray in a linear tapered waveguide.

For the third-order polynomial taper, we can prevent this optical loss without increasing the device length. As shown in Fig.3.3.7, the incident angle of the ray is always large and never becomes small than the critical angle. The slope of the taper can be gradually increased with z, and by this way we can reduce the taper length.

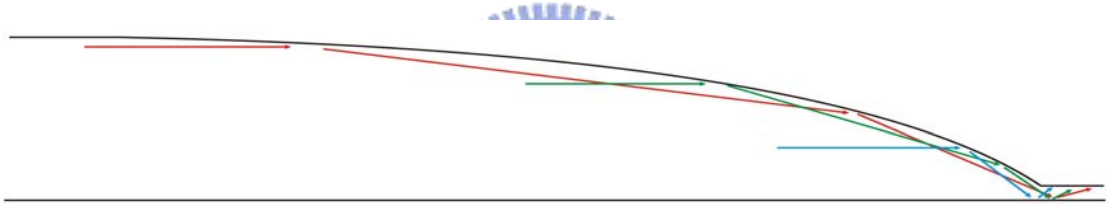

Fig. 3.3.7: Optical ray path in the third- order polynomial taper.

From Fig.3.3.8, we can know that the most sensitive coefficient is a. Now, we estimate fabrication tolerance of our device. In the range of $a=0.524\pm0.05$, we have transmittance more than 90%. Coefficient *a* is the third order coefficient and $0.2 \le h \le 3$ (equation3-12). We can say that we can still have high transmittance with the distortion within about 200nm (from $\Delta a \cdot \bar{h}^3 = 0.05 \cdot (\frac{3+0.2}{2})^3$).

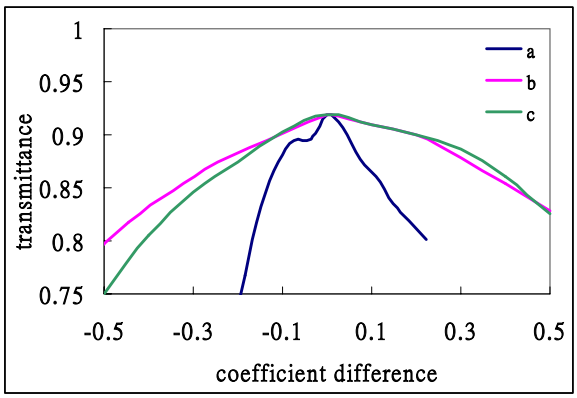

Fig. 3.3.8: The transmittance of our device with different coefficient value.

3.3.4 Summary

In order to increase the coupling efficiency between an integrated optic circuit chip and a single-mode fiber, we propose and design a third-order polynomial tapered waveguide to yield high transmittance and compact size simultaneously. We adjust the coefficients of the polynomial by using a global optimization solver.

After optimization, we obtain a tapered waveguide with the transmittance as high as 91.9% and the taper length only 19.6 μm. By comparing with an optimized linear taper, we verify our nonlinear profile design can effectively reduce the taper length while improve the transmittance.

3.4 UV LED-excited Phosphor White Light Generator with Omni-reflector

3.4.1 Introduction

White light LED (Light Emitting Diode) becomes the most potential light source recently. It exhibits several advantages, such as high energy-utilization efficiency, low heat dissipation, long life time, fast response time and compact size. It saves electricity because of the low driving current and driving voltage. At the present time, the most general light popular is fluorescent light. But some disadvantages of the lighting device can be found, such as brittle, short life time and pollution of mercury. From this point of view, development of white light LED could contribute to environmental protection. However, current luminous efficiency of white light LED is lower than fluorescent light and the cost is still not low enough. The primary applications for LED are limited to LED display and LCD back light.

From lighting point of view, the emissive characteristics of LED still belong to narrowband. Many methods had been proposed to generate white light with LED. We can categorize these methods into the following two groups: Single Die and Multi Dies white light LED.

Single-Die White Light LED:

In this kind of white light LED, a short wavelength LED is used to excite phosphors to generate other wavelength of light. Energy can be lost during the process of excitation. Thus, the luminous efficiency resulting from this technique is typically lower than multi die white light LED.

Currently two schemes of single-die white light LED technology are widely used:

-Blue LED + Yellow Phosphor:

This is the primary method to manufacture white light LED. Blue light excites phosphor to emit yellow light, and the two colors of light will combine to form white light.

-purple (or UV) LED + phosphor:

Using purple or UV LED to excite red, green, and blue phosphors. The three kinds of lights will then combine to form white light. In the same way, other colors of light can also be generated by adjusting the combination of three kinds of phosphor.

Multi-Dies White Light LED:

Multi-dies white light LED uses different colors of LED to generate white light. For example, white light can be generated by using red, blue, and green LEDs or by using complementary colors, such as bluish-green and amber. However, the temperature effect, life time, and intensity for each LED are different. For this reason, the design of driving circuit is complicated that increases the cost.

In this section, we try to use an omni-reflector to enhance the luminous efficiency of a single-die white light LED with purple LED light source and R/G/B phosphors. An omni-directional dielectric mirror exhibits high reflectivity at all angles of incidence and for all states of incident polarization. Unlike metallic mirrors, which absorb a small fraction of incident light, dielectric reflectors are lossless. These properties make omni-reflector an ideal candidate for our design.

3.4.2 Design and Optimization

The schematic of our design is shown in Fig.3.4.1. In order to increase the luminous efficiency, we use an omni-reflector for the wavelength of LED light source, which is assumed to be a purple light LED at wavelength of 405nm. By using omni-reflector, light with wavelength of 405nm will be confined within the device and continuously excite the phosphor to generate white light as shown in Fig.3.4.1 (a). Since no short wavelength photons can leave the device, the optical elements outside the omni-reflector can be made from polymer materials to save the fabrication cost. The light generated by phosphor passes through the purple light omni-reflector as shown in Fig.3.4.1 (b). Therefore, we need an omni-reflector for wavelength of 405 nm but highly transmissive from 470 nm to 700nm.

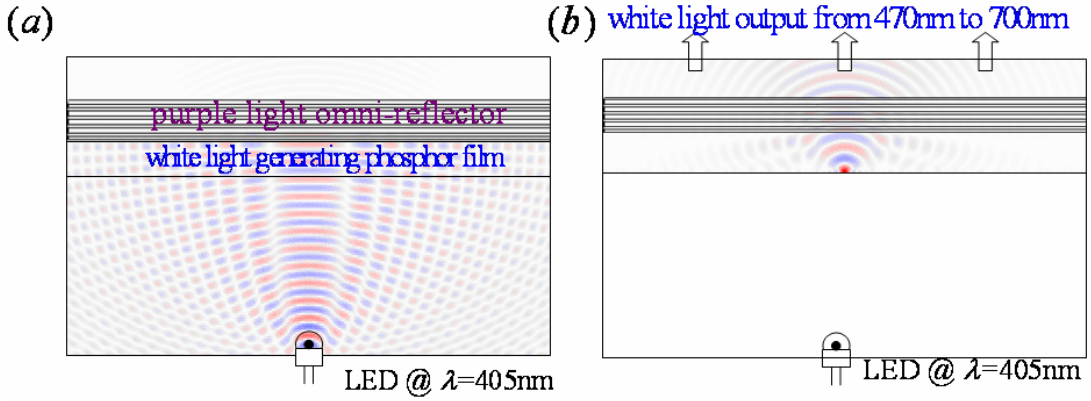

Fig. 3.4.1: Schematic of our design. An omni-reflector is highly reflective for all incident angles and polarization states at the wavelength of 405 nm. The reflector must also be highly transmissive from 470nm to 700nm.

We start our design of an omni-reflector by using a traditional structure of multilayer dielectric mirror. However, the multilayer dielectric mirror is usually very sensitive to the incident angle, as shown in Fig.3.4.2. For a metallic mirror, it can reflect light over a broad range of incident angles but the emissive light from

phosphor can hardly passes through the mirror. Multi dielectric layers omni-reflectors do not have such a problem.

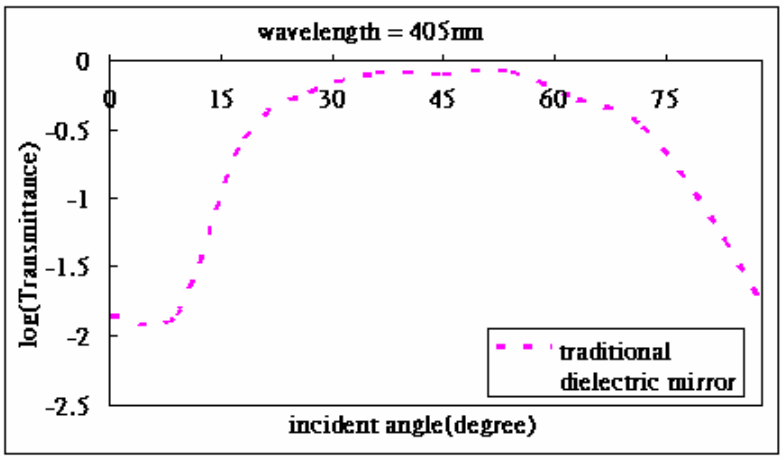

Fig. 3.4.2: Transmittance of a traditional dielectric mirror is plotted as a function of incident angle.

An omni-reflector is a periodic stack of bi-layers, each bi-layer consisting of a high index and a low index dielectric layer as depicted in Fig. 3.4.3. The materials we choose are TiO_2 and SiO_2, which are the most popular optical coating materials with refractive index of 2.59 and 1.47, respectively, at wavelength of 405nm.

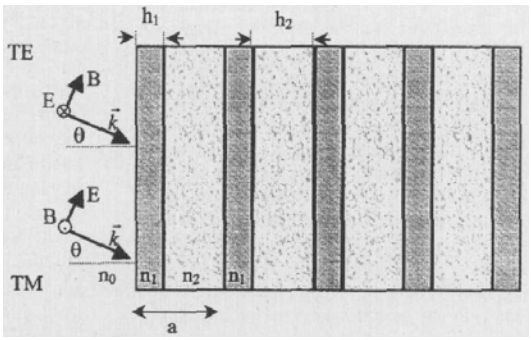

Fig. 3.4.3: Periodic stack of bi-layers, each bi-layer consisting of a high index and a low index dielectric layer.

The ability of a dielectric structure to reflect light with arbitrary angle of incidence has been associated with the existence of a photonic band gap as shown in

Fig.3.4.4. The hashed region indicates the photonic band gap.

The thicknesses (h_1 and h_2) of an omni-directional dielectric mirror can be easily estimated from the equations [18]:

$$\omega_h \approx \frac{2c}{h_2 n_2 + h_1 n_1}\cos^{-1}\left(-\left|\frac{n_1 - n_2}{n_1 + n_2}\right|\right)$$
$$\omega_l \approx \frac{2c}{h_2\sqrt{n_2^2 - n_0^2} + h_1\sqrt{n_1^2 - n_0^2}}\cos^{-1}\left(\left|\frac{n_1^2\sqrt{n_2^2 - n_0^2} - n_2^2\sqrt{n_1^2 - n_0^2}}{n_1^2\sqrt{n_2^2 - n_0^2} + n_2^2\sqrt{n_1^2 - n_0^2}}\right|\right), \quad (3\text{-}13)$$

where ω_h and ω_l denote the frequency limits of the omni-reflection range. Here we set ω_h and ω_l to the wavelength of 365 and 410nm then deduce the thicknesses of h_1=57 and h_2=45 nm. The resulting band structure is shown in Fig. 3.4.4. The dimensionless frequency a/λ for 405nm is about 0.25 which lies in the first hashed region of Fig.3.4.4. The first band gap covers from 370 nm to 505nm.

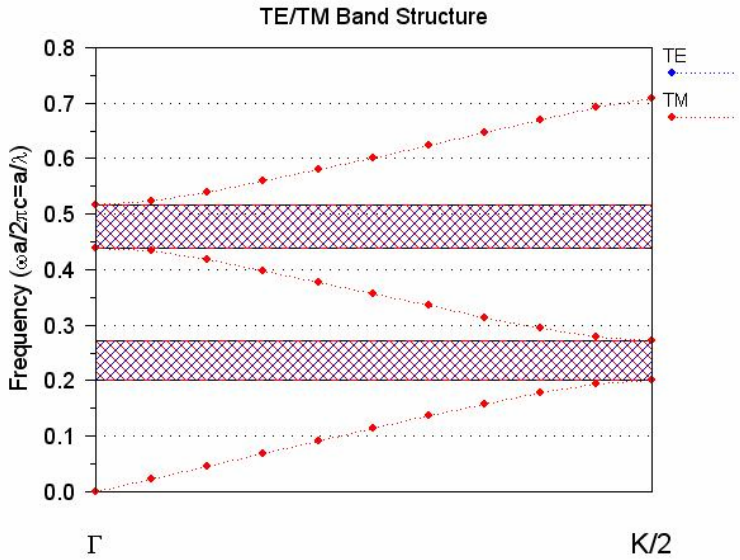

Fig. 3.4.4: Band structure of a periodic multilayered dielectric mirror. The hashed region is the photonic band gap.

From the equations we are not sure that whether the generated light from phosphor can pass through the purple light omni-reflector. For this reason, we search

the layer thicknesses of omni-reflector obtaining from Eq. (3.13) based on the following cost function

$$\text{cost function} = \sum_i [6 \cdot (T_i^{405}) + \sum_j (1 - T_i^j)]. \qquad (3\text{-}14)$$

Here *j* denotes different wavelength of incident light, and *i* indicates different incident angles. Three wavelengths of 480, 590, and 650 nm and five incident angles of 9° , 27°, 45°, 63°,and 81° are chosen. Note that the dispersion of TiO_2 is significant in visible light range and we therefore have to take it into account the material dispersion.

After optimization, we obtain h_1=71 and h_2=129 nm, and the transmittance curves for LED light at 405 nm and the generated light from phosphor are presented in Fig. 3.4.5.

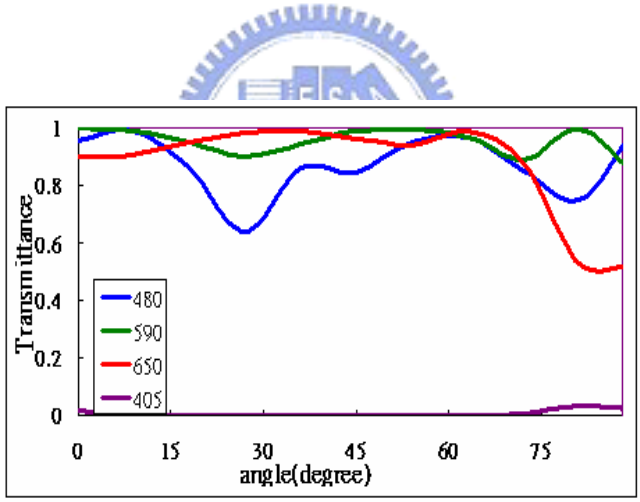

Fig. 3.4.5: The transmittance curves of the optimized omni-reflector for the LED light and the phosphor-generated light.

We also estimate the total transmittance of our design by using a device simulator by assuming the light beam from LED to be a Gaussian beam with a small spot size as shown in Fig.3.4.1 (a). The divergent Gaussian beam can properly simulate the effect of varying incident angles on omni-reflector. The result is shown in Fig.3.4.6. The optical power from 470 nm to 700nm for both TE and TM polarization

has transmission efficiency higher than 80% through the purple light omni-reflector.

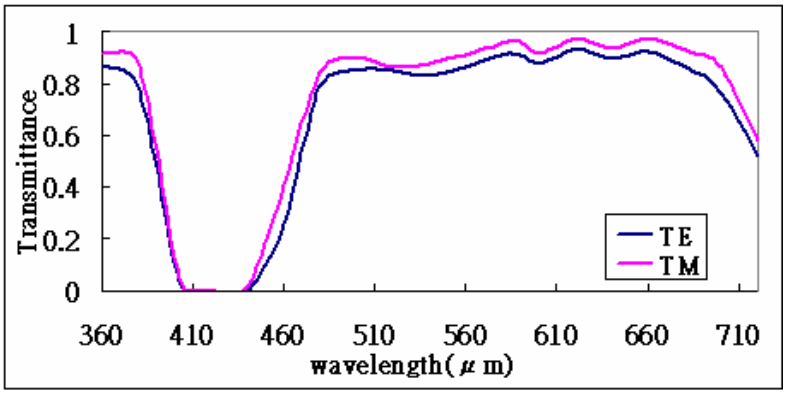

Fig. 3.4.6: Calculated transmittance spectra of our omni-reflector design

3.4.3 Discussion

The transmittance curves at wavelengths of 405, 480, 590, and 650 nm for the optimized and before-optimized omni-reflector are shown in Fig.3.4.7 and Fig.3.4.8. Device optimization retains the high reflectance feature at 405nm, but improves the transmittance of white light.

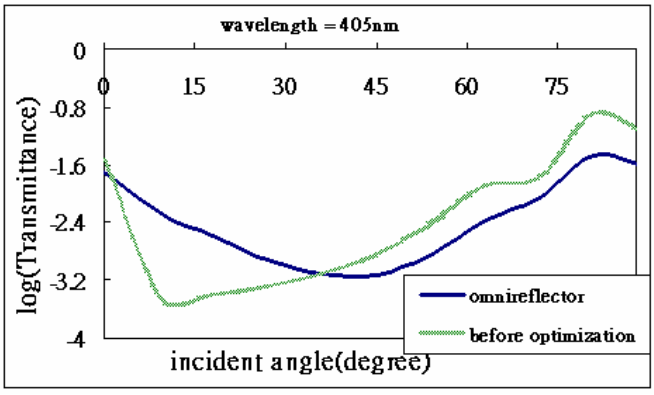

Fig. 3.4.7: The transmittance curves at wavelength of 405nm for the optimized and before-optimized omni-reflector

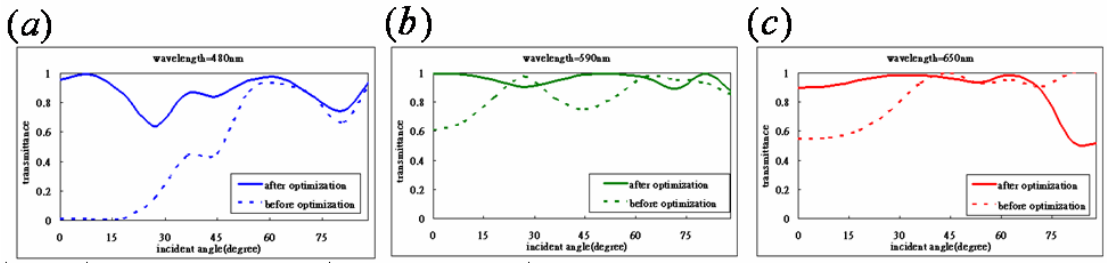

Fig. 3.4.8: The transmittance curves at wavelengths of (a) 480, (b) 590, and (c) 650nm for the optimized and before-optimized omni-reflector.

The band structure of the optimized omni-reflector is shown in Fig. 3.4.9. The dimensionless frequency a/λ for 405nm is about 0.49, which is in the second band gap (hashed region) of Fig.3.4.9. The second band gap ranges from 399 nm to 474 nm, which is narrower and lies in the shorter wavelength region than that of the before-optimized omni-reflector (Fig. 3.4.4). The transmittance of the generated white light is higher for the optimized reflector since the wavelength range of the generated light lies further from the band gap. Note that the real band gap is narrower because of the significant dispersion of TiO_2.

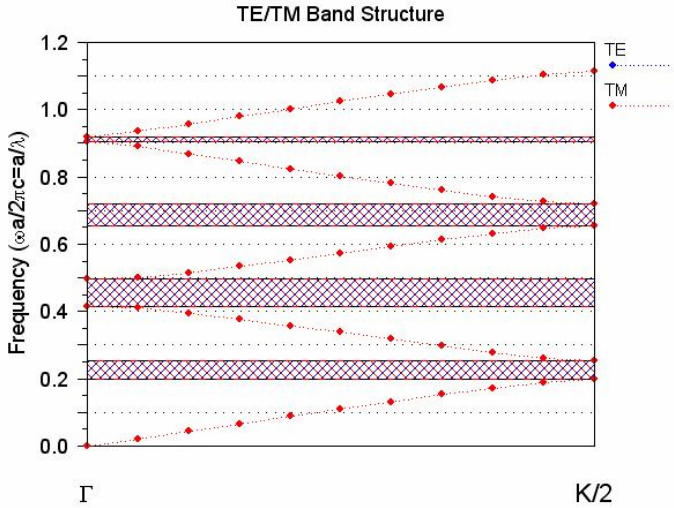

Fig. 3.4.9: Band structure of the optimized omni-reflector.

We now test the fabrication tolerance of device. Fig.3.4.10 shows the

transmittance of the reflector for the wavelength of 405nm with different h_1 and h_2. In order to keep omni-reflect property for wavelength of 405nm, the distortion must be within several nanometers.

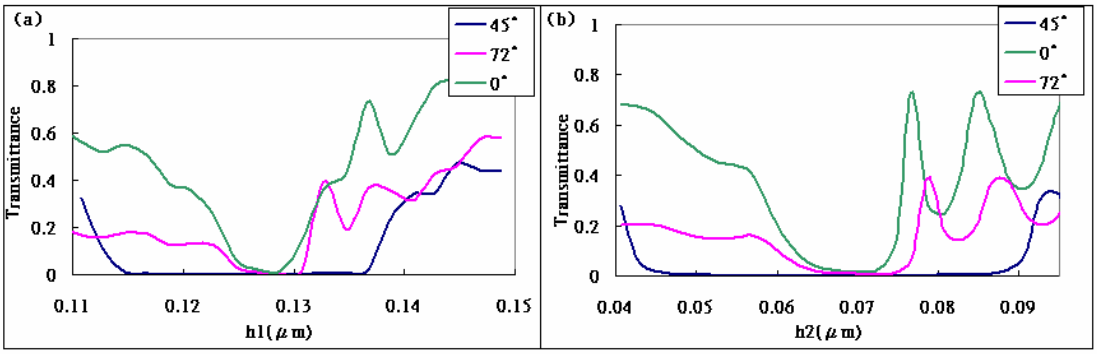

Fig. 3.4.10: Transmittance of the reflector for the wavelength of 405nm with different values of h_1 and h_2.

3.4.4 Summary

In Fig.3.4.1, we propose to use an omni-reflector to increase the luminous efficiency of a white light LED. In order to increase the transmittance of the generated white light, we optimize the thicknesses of the reflector. After optimization, the transmittance of the generated white light is found to be successfully improved while the purple light remains in low transmittance.

Global optimization is a tool which can meet our application requirements. Furthermore by specifying a proper cost function for global optimization, we can change our structure parameters to meet any application.

Chapter 4
Preliminary Experimental Exploration for Magneto-Optical Characterization of Sub-Wavelength Photonic Structures

4.1 Introduction

Optical birefringence generated from nano structures can yield new functionality for photonic applications. The optical anisotropic effects at the nanometer scales are an interesting subject closely relates to SOW devices. In order to provide the sufficient information for this new field, it is highly demanded to develop a sensitive probe to reveal weak optical anisotropy at the nanometer scales. This chapter reports such an effort with some preliminary results. The effect used for this study is focused on the magneto-optical effect. However, the skills developed from this effort can readily be extended to other different effects.

Magneto-optical effect occurs in media in a magnetic field. Faraday first discovered this effect in a glass rod with a magnetic field applied along the direction of propagation of an optical beam. However, the effect is extremely weak in *non-magnetic* media. In magnetic materials (such as ferro-magnetic or ferri-magnetic) the effect can be much larger. Faraday Effect describes the effect observed in optical transmission through a material, while Kerr effect depicts the effect observed on reflection from the surface of a material.

There are three different kinds of experimental geometries for revealing magneto-optical Kerr effect: the polar orientation, the longitudinal orientation, and the transverse orientation which are shown in Fig. 4.1, respectively. In this chapter, we shall focus on the longitudinal case only.

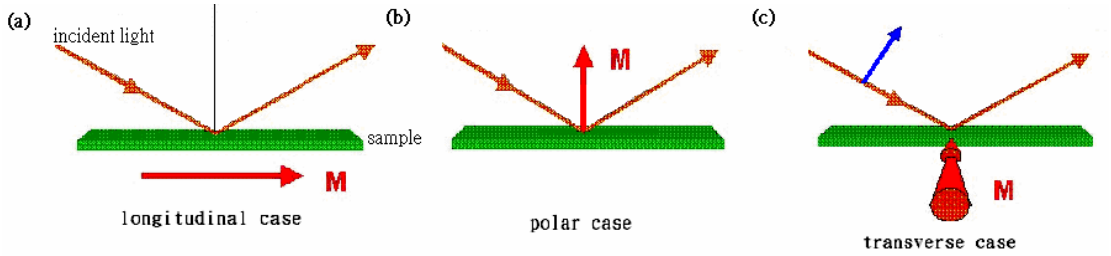

Fig. 4.1: (a) Longitudinal, (b) polar, and (c) transverse orientation of magneto-optical Kerr effect.

Faraday and Kerr effects were shown to be proportional to the magnetization of a sample. Thus, they were used to probe the characteristics of magnetic thin film. Some analytical tools based on magneto-optical Kerr effects include hysteresis loop plotting, magnetic domain imaging, and magneto-optic recording.

4.2 Theory

In the longitudinal case the magnetization vector is in the plane of the surface and parallel to the plane of incidence. The effect occurs with light incidence in either the P-plane (E-vector parallel to the plane of incidence) or the S-Plane (E-vector perpendicular to the plane of incidence). The effect is that the reflected light from light incident in either of P and S linearly polarized states is converted to elliptically polarized light [20]~[21].

The diagram shown in Fig. 4-2 describes the longitudinal geometry. Here you can see the E-vector of the incident beam lies in the S-plane. The amplitude is normalized to be unity for convenience. To the first-order approximation, the reflected E-field consists of two orthogonal components. One is larger and denotes the usual Fresnel amplitude reflection coefficient **r.** The other is smaller and is called the Kerr coefficient k.

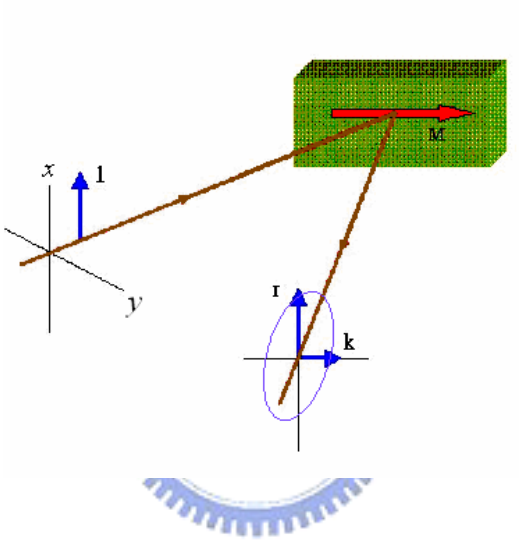

Fig. 4.2: The longitudinal Kerr effect with incident light polarized in the S-Plane

The combination of the two orthogonal components r and k with nonzero mutual phase delay leads to an elliptically polarized optical beam. The major axis of the resulting ellipse is rotated slightly with respect to the principal plane and this is referred to as the Kerr rotation θ_k. There is an associated ellipticity for the ellipse and is called the Kerr ellipticity ε_k. The sign and magnitude of these two parameters are proportional to the magnetization vector M. We should note that r and k need not necessarily be in phase.

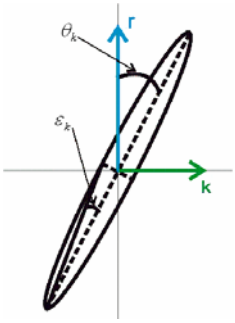

Fig. 4.3: Kerr rotation and Kerr ellipticity of the elliptically polarized light reflected from a material surface.

The complex Kerr rotation can be defined as (k<<r);

$$\tilde{\theta} = \theta_k + i\varepsilon_k = \frac{k}{r} \quad , \qquad (4\text{-}1)$$

where $\theta_k = \mathrm{Re}[\frac{k}{r}]$ is the Kerr rotation angle and $\varepsilon_k = \mathrm{Im}[\frac{k}{r}]$ is the Kerr ellipticity. Both of the parameters are proportional to the sample magnetization. Thus the Kerr rotation of the reflected light can be measured to reveal the variation of the sample magnetization.

4.3 Auto-balanced detection

Since the magneto-optical Kerr effect (MOKE) is extremely weak, we try to improve our detection by combining photoelastic modulation (PEM), lock-in detection and auto-balanced photodetection techniques.

We introduce the auto-balanced photodetection method first. Circuit diagram for the method is shown in Fig. 4.4.

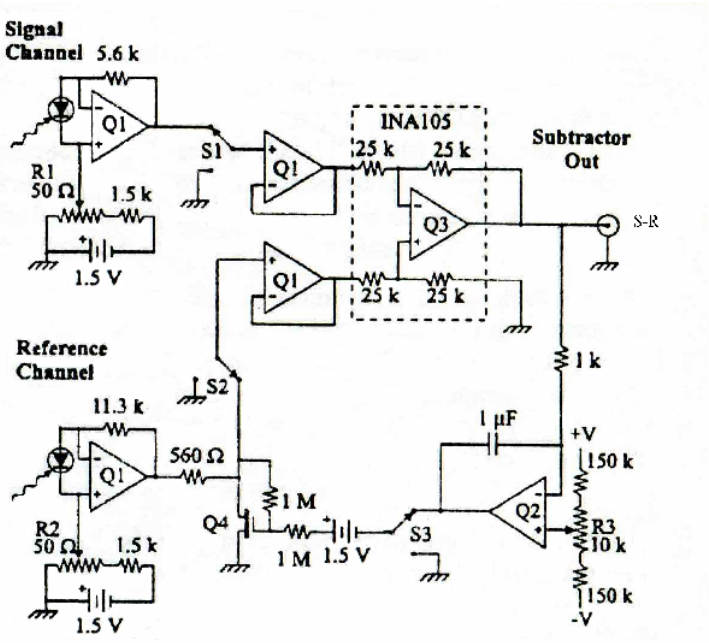

Fig. 4.4: Circuit diagram for the auto-balanced detector. The following components are used: Q1-OP470 a low-noise quad op-amp, Q2-LF356 op-amp, Q3-INA105 precision unity gain differential amplifier, and Q4-2N5457 MOSFET.

The detection circuit consists of two photodiodes. Each photodiode output is sent into a trans-impedance amplifier, where the photocurrent is converted to voltage, and then is amplified. An offset controlled by R1and R2 is produced. The reference channel voltage in the Fig.4.4 goes through a feedback-controlled voltage divider before being subtracted from the signal voltage in Q3. A portion of the output is sent to an integrator, whose result controls the voltage divider. The integrator sets the divider in such a way as to reduce the DC in the subtracted output to zero, thereby achieving balanced detection operation. By subtracting out the signal from the reference channel, the resulting signal also cancels out the noise and improves precision of detection.

The main function of the circuit is to zero out DC term of the signal and cancel out noises. However, since we use lock-in amplifier to detect the modulated (modulated by PEM) MOKE signal, zeroing the DC term of signal in our detector is no longer crucial.

To characterize our auto-balanced circuit, we first conduct some measurements. The first measurement is to demonstrate the cancellation of a large common-mode signal. As shown in Fig. 4.5, a mechanical chopper is used to generate the common-mode signal, which is to be detected with the signal and reference photodiodes. A Wollaston prism is used to separate the incident laser beam into two parts based on the polarization state of the incident light field. We use a polarizer to control the splitting ratio of the input beam.

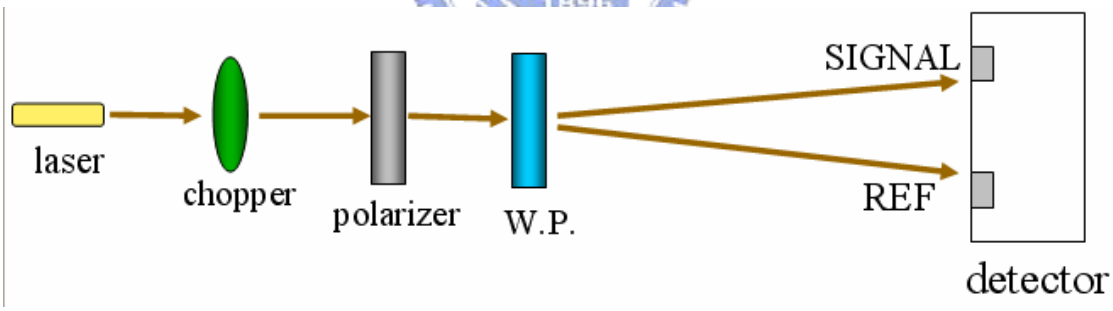

Fig. 4.5 Experimental setup to demonstrate the auto-cancellation for a large common-mode signal.

As shown in Fig.4.6, the common-mode signals generated from the chopper are successfully cancelled out with our auto-balanced detection circuit. Here Fig.4.6 (a) presents the original signal detected by a single photodiode, and Fig. 4.6 (b) is the (S-R) output from our auto-balanced photodetection circuit. The cancellation ability is

dependent on the intensity ratio of the reference and signal input channels. As shown in Fig.4.6 (c), the intensity ratio of the reference and signal input for the best performance is around 0.7. Our auto-balanced detection scheme has been shown to be capable of effectively canceling out a large common-mode signal. In the next test, we shall show that the circuit is also capable of canceling out common noises, such as laser intensity noise appearing in reference and signal inputs.

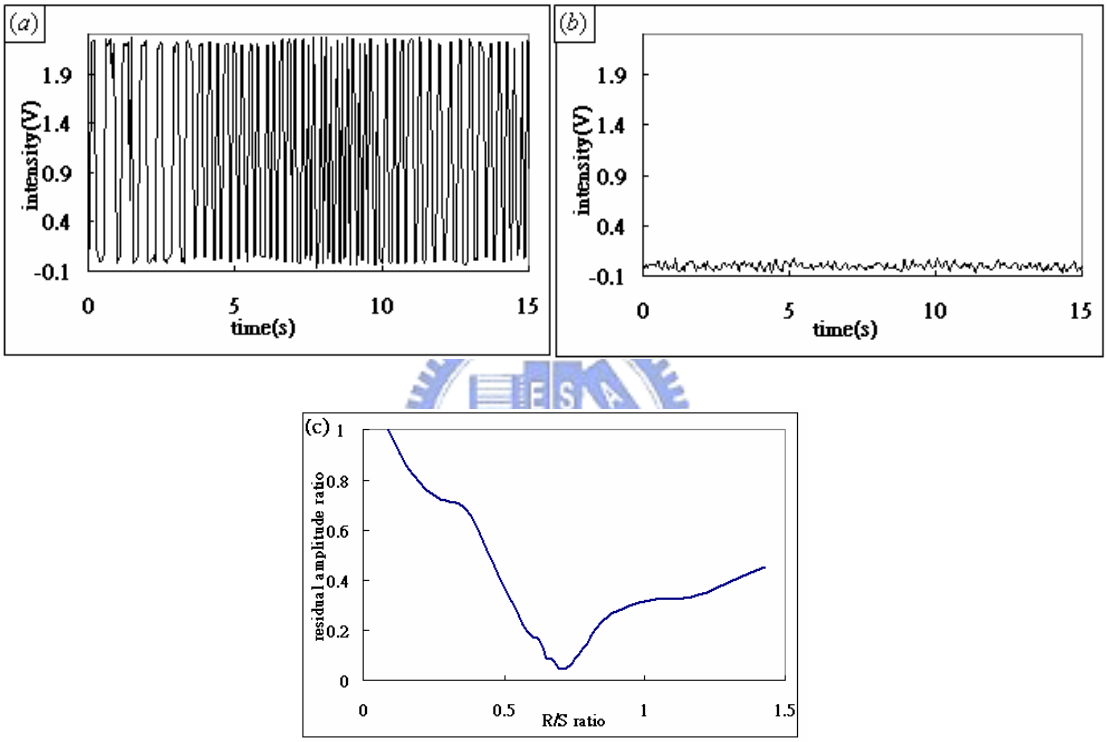

Fig. 4.6 Cancellation ability of our auto-balanced detection circuit. Here the modulating signal to be measured is prepared by a mechanical chopper and is detected with (a) a single photodiode, and (b) the auto-balanced photodetection scheme. (c) The cancellation property is measured as a function of the intensity ratio of the reference and signal inputs.

The schematic diagram of the second experimental arrangement is shown in Fig. 4.7. Similar to the first setup, the Wollaston prism is used to separate the input laser beam into two parts based on the polarization state. The polarizer is used to control the intensity ratio of the splitting beams. The P-polarized beam is directed to incident at the reference input, while the S-polarized beam is directed to incident on a liquid crystal cell. The orientation of the analyzer is oriented to along the horizontal direction that passes P-polarized light. The liquid crystal cell behaves like a quarter-wave plate (without an applied electric field) that converts an S-polarized beam into P-polarized. When an electric field is applied on the LC cell, the optical anisotropy of the cell disappears and no light can pass through the analyzer. We apply a sinusoidal ac field with a frequency of 2-kHz with amplitude modulation at a frequency of 1-Hz by using a function generator. The waveform of the applied electric field is shown in Fig. 4.8 (a). The amplitude of the applied electric field is very low to result in a small signal variation at the signal input of our auto-balanced detector.

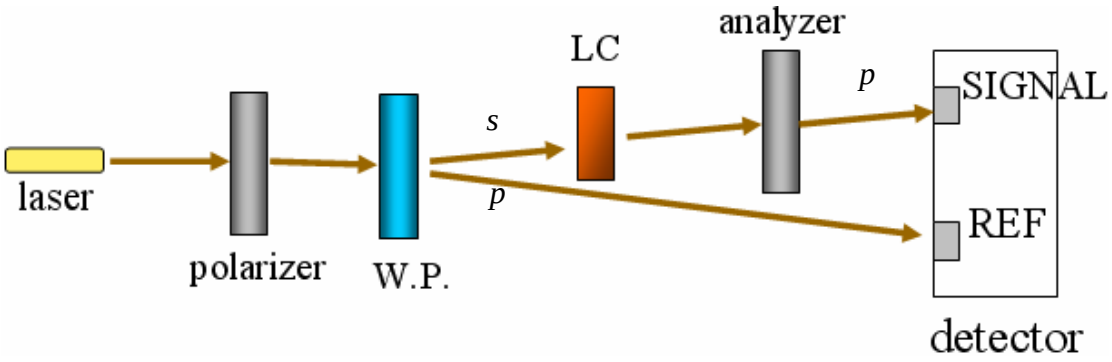

Fig. 4.7 Schematic diagram of the experimental setup used to demonstrate a cancellation effect of noise at a low signal level.

The experimental result is shown in Fig. 4.8 (b) and (c). Note that the intensity detected with single photodiode slightly drifts upward due to an unstable laser output. No such signal drift was found with the auto-balanced detection scheme. In addition, the noise level is clearly lower when the auto-balanced detection scheme is used.

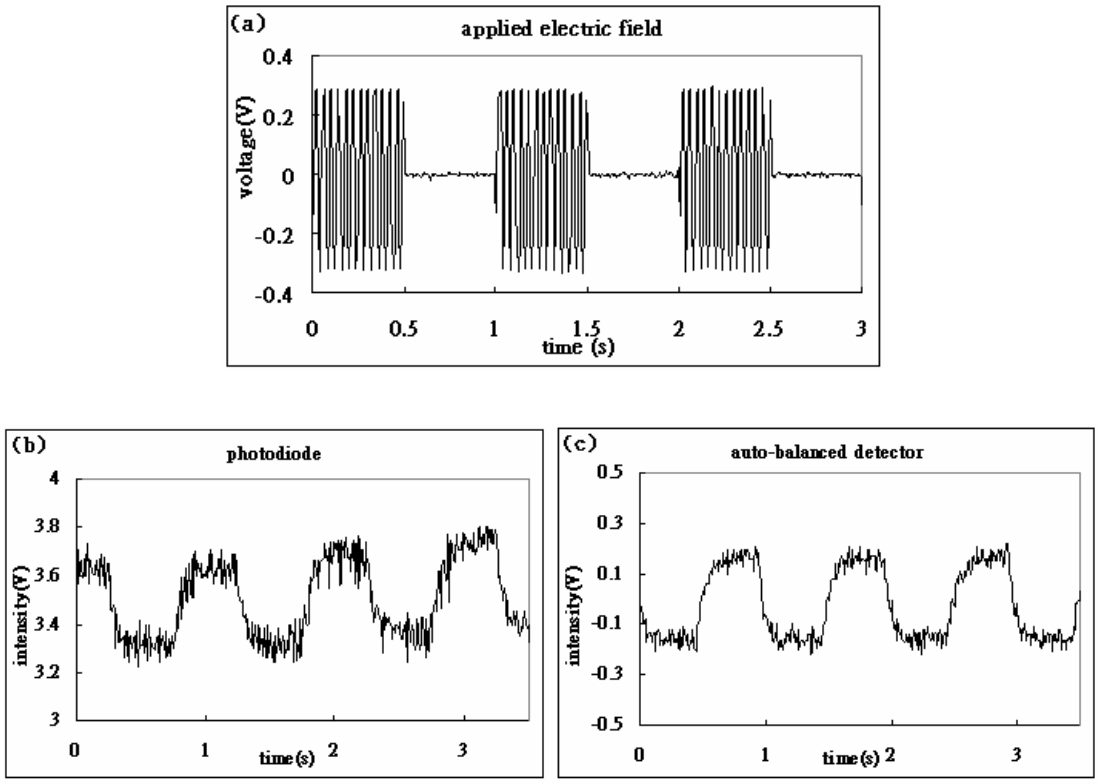

Fig. 4.8 (a) Waveform of the ac electric field applied on the liquid crystal cell. (b) Signal detected by single photodiode. (c) Signal detected with the auto-balanced detection scheme.

4.4 Experimental Setup and Results

Schematic diagram of the preliminary experimental setup for measuring magneto-optical Kerr signal is presented in Fig. 4.9. The Wollaston prism splits the

incident beam into two parts with polarizations orthogonal to each other. One beam is brought to incident on the reference detector, and the other beam is used for the signal arm. The polarizer is orientated to along the x-axis (0°), which allows S-polarized light to pass. The reflected light is elliptically polarized by the sample to yield two orthogonal components r and k from the magneto-optical Kerr effect. Note that the k-component is usually very small. Thus we shall use PEM to modulate the signal and retrieve the weak modulated k component with a lock-in amplifier.

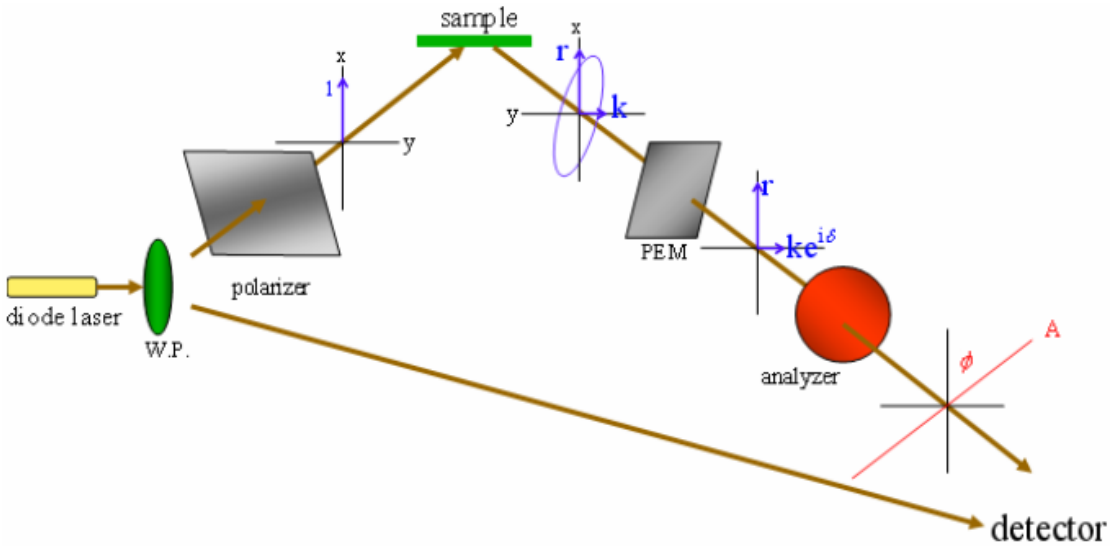

Fig. 4.9 Schematic diagram showing the experimental setup for probing the magneto-optical Kerr effect of a test sample.

The setup of Fig. 4.9 can be analyzed with Jones calculus. By setting the orientations of polarizer and analyzer to be 0° and 45°, the signal field can then be derived to be

$$
\begin{aligned}
\mathrm{E_f} &= \begin{bmatrix} E_y \\ E_x \end{bmatrix} = \mathrm{A \cdot M \cdot S \cdot P \cdot E_i} \\
A &= \frac{1}{2}\begin{bmatrix} 1 & -1 \\ 1 & 1 \end{bmatrix}\begin{bmatrix} 1 & 0 \\ 0 & 0 \end{bmatrix}\begin{bmatrix} 1 & 1 \\ -1 & 1 \end{bmatrix} \\
M &= \begin{bmatrix} 1 & 0 \\ 0 & e^{i\delta} \end{bmatrix} \quad , \qquad \text{(4-2)} \\
S &= \begin{bmatrix} \tilde{r}_{pp} & \tilde{r}_{ps} \\ \tilde{r}_{sp} & \tilde{r}_{ss} \end{bmatrix} \\
P \cdot E_i &= \begin{bmatrix} 0 \\ 1 \end{bmatrix} \cdot E_0
\end{aligned}
$$

where A, M, S, and P denote the Jones matrices of analyzer, PEM, sample, and polarizer, respectively. The signal field can be simplified to be

$$
\mathrm{E_f} = \frac{E_0}{2}\begin{bmatrix} \tilde{r}_{ps} + \tilde{r}_{ss} e^{i\delta} \\ \tilde{r}_{ps} + \tilde{r}_{ss} e^{i\delta} \end{bmatrix}, \qquad \text{(4-3)}
$$

where $\delta = \delta_0 \sin \omega t$ represents the modulation effect of PEM with ω being the modulation frequency and δ_0 the modulation depth. When δ_0 is sufficient small, $e^{i\delta}$ can be expanded as

$$
e^{i\delta} = \cos\delta + i\sin\delta \approx J_0(\delta_0) + 2J_2(\delta_0)\cos 2\omega t + i[2J_1(\delta_0)\sin\omega t]. \qquad \text{(4-4)}
$$

The modulated signal intensity becomes

$$
I = \left|E_f\right|^2 \approx \left|\tilde{r}_{ss}\right|^2 + 2J_1(\delta)\left|\tilde{r}_{ss}\right|^2 \varepsilon_k \sin\omega t + 2J_2(\delta)\left|\tilde{r}_{ss}\right|^2 \theta_k \cos 2\omega t \quad , \qquad \text{(4-5)}
$$

where the Kerr rotation angle is $\theta_k = \mathrm{Re}[\frac{r_{ps}}{r_{ss}}]$ and $\varepsilon_k = \mathrm{Im}[\frac{r_{ps}}{r_{ss}}]$ denotes the Kerr ellipticity. Therefore from Eq. (4.4), we can find that the Kerr ellipticity and Kerr rotation relate to the measured ω- and 2ω-signal components of the reflected light.

To improve the detection sensitivity of MOKE signal, the modulation depth of PEM shall be properly adjusted and the orientation of analyzer shall be oriented to a proper direction. This condition can be fulfilled by first setting the orientation of the polarizer to 45° and the modulation depth to be 3.2 rad. By using a polished silicon wafer as the reference sample, the two components of the reflected light are large and the MO-induced depolarization effect can be neglected. The modulated signal is the y-component of the reflected light. We then adjust the orientation of the analyzer to maximize the modulated signal. The simulated result is shown in Fig. 4.10 (a). We can see that the maximum signal can be achieved with the analyzer orienting at 45°. We can go further to adjust the modulation depth by first setting the transmission axis of the analyzer to be 45° and measuring the signal as a function of modulation depth. The calculated result is shown in Fig. 4.10 (b). We can find that for the detection of 2ω-signals the optimal modulation depth is 2.9 rad with an orientation angle of 45° for the analyzer.

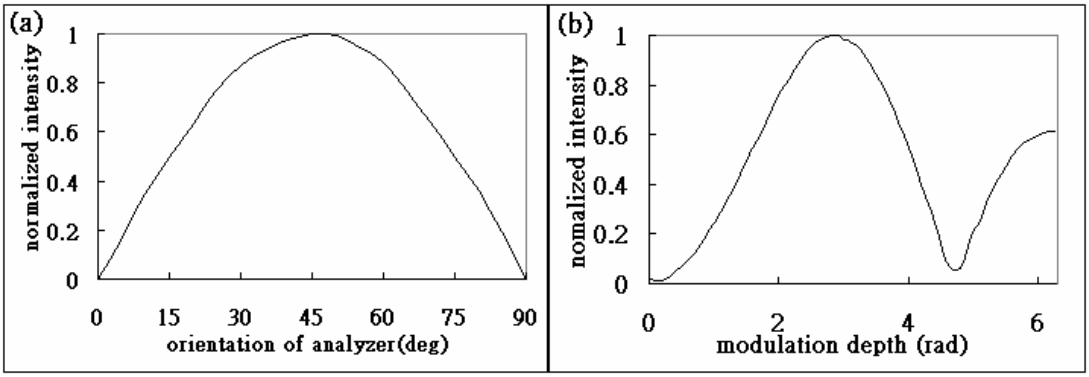

Fig. 4.10 (a) Variation of modulated signal intensity as a function of the analyzer orientation. (b) Intensity variation of the modulated signal at 2ω as a function of modulation depth.

Recently nano-structured magnetic materials have attracted significant interests in both fundamental research and applied technologies. This is because enhanced and tailorable magnetic properties from known materials could be achieved with nanotechnology. Magnetization hysteresis loop measurement can provide rich information for both scientists and engineers. We apply our setup for investigating the magnetic response of a film of ZnO quantum dots doped with 0.7% Co^{2+}. The quantum dots are dissolved in ethanol and the film can be formed by spreading the solution drop-by-drop on the silicon wafer and heating the sample to 40°C to evaporate the solvent. The measurement result of the hysteresis loop is shown in Fig. 4.11. It is amazing to find that the magnetization loop persists even at room temperature, indicating the film of 0.7% Co^{2+}-doped ZnO quantum dots to be ferromagnetic at room temperature. The Kerr rotation from the MOKE effect is as small as 1×10^{-5} rad, which also reflects the detection sensitivity of setup shown in Fig. 4.9.

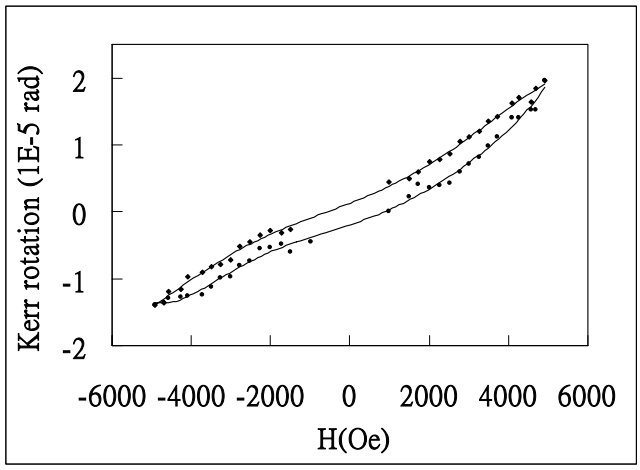

Fig. 4.11 Measured magnetization hysteresis loop of ZnO quantum dots doped with 0.7% Co^{2+} by our MOKE measurement apparatus.

We further present the measurement results of the noise level in our MOKE detection apparatus. Measurement results at zero magnetic field are shown in Fig. 4.12. The root mean-square error is found to be 0.066 (10^{-5} rad) with a detection scheme of single photodetector and 0.057 (10^{-5} rad) for the auto-balanced detection method. The noise influence is not significantly reduced with auto-balanced detection scheme since the noise level has been significantly reduced by lock-in detection, which is modulated at 47 kHz by PEM.

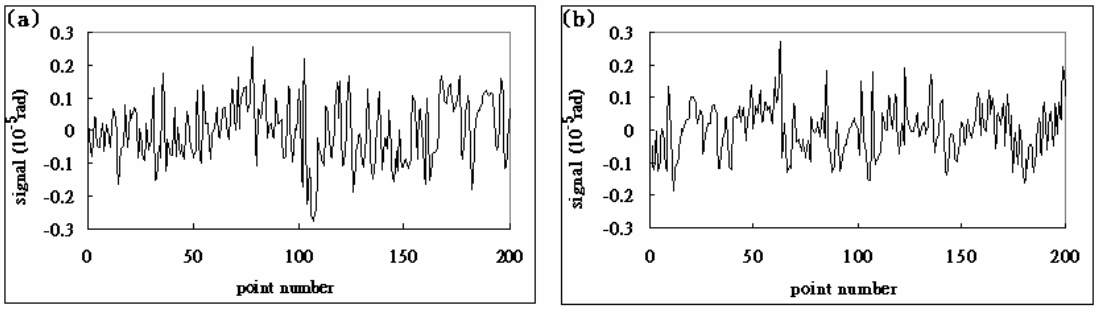

Fig. 4.12 Kerr rotation measurement at zero magnetic field with (a) single photodetector, and (b) the auto-balanced detection method.

4.5 Summary

As shown in section 4.3, auto-balanced detector can cancel out noise influences. However, there is no clear difference in the detection of Kerr rotation when comparing the lock-in measurement results with a single photodetector and the auto-balanced detection method. Auto-balanced detection is supposed to be able to cancel out the noise between reference and signal channels. However, when the noises in both channels are uncorrelated or noise only appears in one of the signal and reference arms, the auto-balanced detection will not be work. Most noises are broadband and can be reduced by using lock-in detection scheme. In our case, the modulated signal with frequency around 94 kHz (2ω) is picked up by lock-in

detection, which significantly reduces the noise level within the lock-in detection bandwidth. For the reason, the auto-balanced detection does not significantly improve the detection sensitivity of our MOKE apparatus with lock-in detection method.

We have achieved a detection sensitivity of Kerr rotation at about 10^{-5} radian. The magnetization hysteresis loop of a film of ZnO quantum dots doped with 0.7% Co^{2+} had been successfully obtained. Hysteresis loop carries the information about the characteristics of a magnetic thin film, such as remanent magnetization, saturate magnetization, and coercive force. The measured magnetization loop of the Co^{2+}-doped ZnO quantum dots persists even at room temperature, indicating the film to be ferromagnetic at room temperature.

Chapter 5
Conclusion and Future Prospect

In the chapter 2 of this thesis, we compare several global optimization solvers. The multi-start-based random search seems to be the most suited one. It offers the correct global minimum during our test run. In addition, during the searching, it also provides other local minima, which may provide us extra information to a clever design of SOW device.

In chapter 3 we reported several applications of global optimizers and device simulator in the optimal design of sub wavelength photonic devices. Global optimization can adjust design parameters to meet our application requirements by specifying a proper cost function for global optimization. Global optimization technique is not only a useful tool to help us discovering the optimal device parameters, but also allows us to discover the operation principle of the device and therefore the design rules.

In view that the optical anisotropic effects at the nanometer scales are an interesting subject closely relates to SOW devices, it is highly desirable to develop a sensitive probe to reveal weak optical anisotropy at the nanometer scales. We in chapter 4 report such an effort with some preliminary results. We describe a preliminary experimental study for probing the magneto-optical Kerr effect in a nano structured magnetic material. We can detect the Kerr rotation with magnitude as small as 10^{-5} radian and the hysteresis loop of the magnetic thin film was successfully acquired.

The future prospect of the thesis research can proceed in the future in two

directions: First, we can fabricate these sub wavelength photonic devices reported in the thesis and other suitable SOW structures with metal or dielectric materials and probe the optical field distribution with near-field microscopy to verify the device function and the detailed distribution of the light field. Secondly, in view that the light field distribution at sub optical wavelength scales is not well understood, there are plenty room for new phenomena can be observed and new functionalities can be employed for advanced photonic devices. By combining the computation-effective global optimization solvers with appropriate device simulators shall offer us opportunity to generate new novel structures for fundamental study and engineering development.

Reference

[1] Horst, Reiner & Tuy, Hoang, Global Optimization :deterministic approaches.

[2] Michael Bass, Eric W. Van Stryland, David R. Williams, William L. Wolfe, Handbook of Optics: Devices, Measurements, and Properties Volume 2, p7.18.

[3] Hattori, K., T. Kitagawa, M. Oguma, Y. Ohmori, and M. Horihuchi.1994. Erbium-doped silica-based waveguide amplifier integrated with a 980/1530 nm WDM coupler. Electron. Lett. 30:856-857.

[4] Negami, T., H. Haga, and S. Yamamoto. 1989.Guided-wave optical wavelength demultiplexer using an asymmetric Y-junction. Appl. Phys. Lett. 54:1080-1082.

[5] Tervonen, A., P. Poyhonen, S. Honkanen, and M. Tahkokorpi. 1991. A guided-wave Mach-Zehnder interferometer structure for wavelength multiplexing. IEEE Photon. Tech. Lett. 3:516-518.

[6] SOLDANO, L.B., and PENNINGS, E.C.M.: 'Optical multi-mode interference device based on self-imaging principles and applications', J. Lightwave Technol., 1995,13,(4), pp.615-627

[7] Li, BJ; Li, GZ; Liu, EK; et al.:' Low-loss 1x2 multimode interference wavelength demultiplexer in silicon-germanium alloy', IEEE PHOTONIC TECH L, 11 (5): 575-577 1999 MAY

[8] Li, BJ; Li, GZ; Liu, EK:' Guided-wave Si1-xGex/Si wavelength demultiplexer based on multimode interference', INFRARED PHYS TECHN, 39 (2): 61-67 MAR 1998

[9] Lin, YJ; Lee, SL:' InP-based 1.3/1.55 mu m wavelength demultiplexer with multimode interference and chirped grating',OPT QUANT ELECTRON, 34 (12): 1201-1212 DEC 2002

[10] Chuang, WC; Chang, CY; Lai, CC; et al.:' Integrated-optics multimode-interference wavelength division multiplexer for optical communication', FIBER INTEGRATED OPT, 18 (2): 93-104 1999

[11] M. Born and E. Wolf, Principles of Optics: electromagnetic theory of propagation interference and diffraction of light (Pergamon, Oxford, 1975), p.705.

[12] Rong-Chung Tyan, Pang-Chen Sun, Axel Scherer, and Yeshayahu Fainman, Opt. Lett. **21,**761(1996)

[13]M. Schmitz, R. Brauer, and O. Bryngdahl, Opt. Lett. **20**, 1830 (1995).

[14]D. Yi, Y. Yan, H. Liu, S. Lu, and G. Jin, Opt. Lett. **29**, 754 (2004).

[15]Kasaya K, Mitomi O, Naganuma M, Kondo Y and Noguchi Y, 1993, "A simple laterally tapered waveguide for low-loss coupling to single mode fibers, IEEE Photon. Technol. Lett. 3 345.

[16]Paulo A. Yazaki, Kazuhiro Komori, Giampaolo Bendelli, Shigehisa Arai and Yasuharu Suematsu, IEEE Transactions Photonics Technology Letters, Vol.3, No.12, December, 1991.

[17]A. F. Milton and W. K. Burns, "Mode coupling in optical waveguide horns." IEEE J. Quantum Electron., vol.QE-13, pp.828-835, Oct. 1977.

[18]S. J. Hettrick, J. Wang, C. Li, J. S. Wilkinson, and D. P. Shepherd, Journal of Lightwave Technology, Vol.22, No. 3, 2004

[19]Y. Fink, J.N. Winn, S. Fan, C. Chen, J. Michel, J. D. Joannopoulos, and E. L. Thomas, Science, Vol. 282, pp.1679-1682, 1998

[20]J. W. Lee, J. R. Jeong, D. H. Kim, J. S. Ahn, J. Kim, and S. C. Shin, Review of Scientific instruments, Vol.71, No. 10, 2000.

[21]Katsuaki Sato, Japanese Journal of Applied Physics, Vol.20, No. 12, December 1981.